

FRONT COVER

GRANT NO. DAMD 17-93-J-3009

TITLE: DIGITAL MAMMOGRAPHY WITH STORAGE PHOSPHORS

PRINCIPAL INVESTIGATOR: Chris C. Shaw, Ph.D.

PI ADDRESS: University of Pittsburgh, Department of Radiology  
A441 Scaife Hall, Pittsburgh, PA 15261

REPORT DATE: December 31, 1994

TYPE OF REPORT: Annual Report

PREPARED FOR: U.S. Army Medical Research and Materiel Command  
Fort Detrick, Frederick, MD 21702-5012

DISTRIBUTION STATEMENT: Approved for Public Release; Distribution  
Unlimited



19950313 057

REPORT DOCUMENTATION PAGE			Form Approved OMB No. 0704-0188
<small>Public reporting burden for this collection of information is estimated to average 1 hour per response, including the time for reviewing instructions, searching existing data sources, gathering and maintaining the data needed, and completing and reviewing the collection of information. Send comments regarding this burden estimate or any other aspect of this collection of information, including suggestions for reducing burden, to Washington Headquarters Services, Directorate for Information Operations and Reports, 1215 Jefferson Davis Highway, Suite 1204, Arlington, VA 22202-4102, and to the Office of Management and Budget, Paperwork Reduction Project (0704-0188), Washington, DC 20503.</small>			
1. AGENCY USE ONLY (Leave Blank)	2. REPORT DATE 12/23/94	3. REPORT TYPE AND DATES COVERED Annual 12/01/93-11/30/94	
4. TITLE AND SUBTITLE  DIGITAL MAMMOGRAPHY WITH STORAGE PHOSPHORS		5. FUNDING NUMBERS Grant DAMD17-93-J-3009	
6. AUTHOR(S)  Chris C. Shaw, Ph.D.			
7. PERFORMING ORGANIZATION NAME(S) AND ADDRESS(ES)  University of Pittsburgh Department of Radiology A441 Scaife Hall Pittsburgh, PA 15261		8. PERFORMING ORGANIZATION REPORT NUMBER	
9. SPONSORING/MONITORING AGENCY NAME(S) AND ADDRESS(ES)  U.S. Army Medical Research and Materiel Command ATTN: MCMR-RMI-S Fort Detrick Frederick, MD 21702-5014		10. SPONSORING/MONITORING AGENCY REPORT NUMBER	
11. SUPPLEMENTARY NOTES			
12a. DISTRIBUTION/AVAILABILITY STATEMENT  Approved for Public Release; Distribution Unlimited		12b. DISTRIBUTION CODE  PB	
13. ABSTRACT (Maximum 200 words)  In the second year of the grant period, we have completed the following tasks: 1. We have improved the spatial resolution capability of our storage phosphor image reader by further reducing the laser spot size from 50 $\mu$ m (obtained in first year) to 40 $\mu$ m. 2. We have measured and compared the MTFs of the improved system with those of commercial systems. 3. We have developed a phantom for monitoring the overall image quality. 4. We have constructed and tested phantoms for the comparison study. 5. We have begun acquisition of storage phosphor and film images for the ROC study. 6. We have completed the test of the compression algorithms developed in the previous year. We have demonstrated with phantom images that the quality of the storage phosphor images, obtained with the improved imaging system, are superior to those obtained with current commercial systems. We have also shown that the quality approaches that of the screen-film images. We anticipate that image acquisition will be completed in January of 1995 and the ROC study will begin in February.			
14. SUBJECT TERMS  Digital Radiography, Mammography, Breast Imaging, Computed Radiography, Storage Phosphor		15. NUMBER OF PAGES 49	
		16. PRICE CODE	
17. SECURITY CLASSIFICATION OF REPORT Unclassified	18. SECURITY CLASSIFICATION OF THIS PAGE Unclassified	19. SECURITY CLASSIFICATION OF ABSTRACT Unclassified	20. LIMITATION OF ABSTRACT Unlimited

NFSN 7540-01-280-5500

Standard Form 298 (Rev. 2-89)  
Prescribed by ANSI Std Z39-18  
276-102

## FORWARD

Opinions, interpretations, conclusions and recommendations are those of the author and are not necessarily endorsed by the U.S. Army.

( X ) Where copyrighted material is quoted, permission has been obtained to use such material.

( X ) Where material from documents designated for limited distribution is quoted, permission has been obtained to use the material.

( X ) Citations of commercial organizations and trade names in this report do not constitute an official Department of the Army endorsement or approval of the products or services of these organizations.

( NA ) In conducting research using animals, the investigator(s) adhered to the "Guide for the Care and Use of Laboratory Animals," prepared by the Committee on Care and Use of Laboratory Animals of the Institute of Laboratory Animal Resources, National Research Council (NIH Publication No. 86-23, Revised 1985).

( NA ) For the protection of human subjects, the investigator(s) have adhered to policies of applicable Federal Law 45 CFR 46.

( NA ) In conducting research utilizing recombinant DNA technology, the investigator(s) adhered to current guidelines promulgated by the National Institutes of Health.

  
\_\_\_\_\_  
PI Signature

Accession For	
STIS GRAIL	<input checked="" type="checkbox"/>
DTIC TAB	<input type="checkbox"/>
Unannounced	<input type="checkbox"/>
Justification	
By _____	
Description _____	
Availability Codes	
STIS	DTIC
Publ	Special

*3*

*A-1*

## TABLE OF CONTENTS

	PAGE NUMBER
1. Cover Page	<u>1</u>
2. SF 298 Report Document Page	<u>2</u>
3. Forward	<u>3</u>
4. Table of Contents	<u>4</u>
5. Introduction	<u>5</u>
6. Body	<u>6-17</u>
7. Conclusions	<u>19</u>
8. References	<u>20-25</u>
9. Appendix	<u>26-32</u>

additional pages : 10-A, 15-A, 15-B, 15-C, 15-D, 18-A, 26-A

additional material : One set of <sup>9</sup>14" x 17" or 7" x 9" films attached  
(see Appendix IV for list and captions)

## INTRODUCTION

### Overall Goals

Although the storage phosphor imaging technique has become a promising candidate for large scale implementation of digital radiography in medium resolution applications such as chest radiography and abdominal imaging<sup>1-7</sup>, it does not have sufficient spatial resolution capability for mammographic imaging applications<sup>92,93</sup>. This is partially due to the limitation of the screen optics<sup>8-10</sup>. A more important cause, which can be resolved, is the use of large laser beam spot size with most commercial storage phosphor image reader<sup>8-13</sup>.

In this project, we propose to modify and optimize an experimental CR system for high resolution mammographic imaging applications. Image properties of the optimized system will be characterized by measuring the signal response, MTF and noise properties. A comprehensive comparison study based on phantoms will be conducted to evaluate and compare the CR technique with the conventional screen-film technique for detection of microcalcifications as well as low contrast soft tissue masses. Possibility for patient dose reduction will also be investigated. In an addendum to our proposal dated October 26, 1992, we also proposed to perform preliminary investigations on data compression of mammographic or similar types of images.

### Main Tasks

The project consists of four major components: (1) system modification and optimization, (2) system characterization and quality control, (3) comparison study and (4) image compression study. To this date, Tasks 1, 2 and 4 have been largely completed although quality control of the system is an ongoing endeavor. Task 3 is about 50% completed. Specific tasks completed in the first and second years are summarized as follows:

In the first year of the grant period, we have begun and completed the following tasks:

1. We modified the laser optics and reduced the beam spot size from 120 $\mu\text{m}$  to 50 $\mu\text{m}$ . We measured and confirmed the reduction of spot size.
2. We measured and compared the resolution capability of the modified imaging system with that of the unmodified system.
3. We investigated the methods of constructing a suitable phantom for later on comparison studies.
4. We implemented and tested several image compression schemes and applied them to digitized mammograms.

In the second year of the grant period, we have accomplished the following tasks:

1. We have improved the spatial resolution capability of our storage phosphor image reader by further reducing the laser spot size from  $50\mu\text{m}$  (obtained in first year) to  $40\mu\text{m}$ .
2. We have measured and compared the MTFs of the improved system with those of commercial systems.
3. We have developed a phantom for monitoring the overall image quality.
4. We have constructed and tested phantoms for the comparison study.
5. We have begun acquisition of storage phosphor and film images for the ROC study.
6. We have completed the test of the compression algorithms developed in the previous year.

Methodology and results for the second year tasks will be described and discussed in the following sections.

## EXPERIMENTAL METHODS

### 1. Further System Improvement

We have continued to improve our experimental storage phosphor imaging system (ESPIS) for better image quality and for more convenient operation. For better spatial resolution properties, we have further reduced the laser spot size from 50 $\mu$ m to 40 $\mu$ m (full width at half maximum). We have also acquired a number of high resolution storage phosphor screens for use in image acquisition for the ROC study. These screens include the newest one from Fuji: HR-V. We have tested and shown that HR-V offers the same spatial resolution quality although a higher light gain.

We have also developed various techniques for measuring the parameters for system operation and performance. For instance, we have improved our technique for measuring the laser beam intensity profile so that it can be used on a real-time basis during the focusing procedure. This involves the development of system software for digitizing, scaling and displaying the laser beam intensity signal at a much faster rate (1 cycle every several seconds). This greatly improves the ease and accuracy of the focusing procedure. As the result, we have been able to reduce the laser spot size from 50 $\mu$ m to 40 $\mu$ m. Further reduction is possible. However, it may start to degrades the sampling process and generate gaps where x-ray information would be lost and image noise may increase. Although we continue to investigate the pros and cons of smaller spot size, we have reached the conclusion that based on practical considerations, it would be a good compromise to use 40 $\mu$ m laser beam spot in our comparison study.

We have also updated the acoustic-optical modulator (AOM) to allow more reliable and less noisy operation. A beam intensity monitor and feedback loop were added to minimize the fluctuation of laser beam power. We have also developed a series of techniques for testing the operation of ESPIS. One of these techniques is direct measurement of the scanning laser intensity pattern. We have been able to use film to monitor and measure the spatial intensity distribution of the scanning laser beam. This technique has proved to be useful in checking the stability of the laser power or the proper function of the AOM.

## 2. Measurement of Image Quality

We have concentrated on the modulation transfer function (MTF) and detective quantum efficiency (DQE) for measurement of the image quality.

### Spatial Resolution

We continued to use a lead bar resolution pattern (Nuclear Associates 07-553) to monitor and measure the spatial resolution quality of the ESPIS. It consists of 22 groups

of bar patterns with a frequency ranging from 0.25 to 10 lps/mm. Each group has a 4 cycle bar pattern. A specification list for the resolution bar pattern is attached as Appendix II.

The bar pattern images are visually examined to evaluate the spatial resolution limit of the imaging system. A fully resolved pattern (with good contrast) generally indicates that the MTF is around 0.05 or greater at that particular frequency. A partially or barely resolved pattern with faint contrast indicates that the MTF is probably between 1% and 5%. Unresolved bar patterns generally indicate that the MTF is below 1%. This observation could vary from person to person but may be used a crude guideline when visually examining the bar pattern images.

The methods for measuring the spatial resolution properties of a storage phosphor imaging system have been previously discussed and demonstrated<sup>8,9,12,13</sup>. Our methods focus on the use a standard resolution test pattern as described before. The square wave response function (SWRF) can be measured by plotting the signal profile across the bar patterns and then measuring the average amplitude for each frequency. Because the square waves contain high order harmonics, the SWRF can not be directly used to compute the MTF without correction for these harmonics. We have devised and tested a signal processing method to compute the MTF from the signal profile of a bar pattern.

The signal profile was first segmented into sections of the same frequency. Sections from a number of lines (20-70) were concatenated together into a big array with many more cycles of change. The array was then Fourier transformed and a frequency distribution of the signals was computed. This frequency distribution typically has a fundamental peak followed by a number of high order harmonics. These harmonics generally decrease in magnitude as the order becomes higher. To determine the MTF value, the peak for the fundamental peak was measured and normalized by dividing it by the zero frequency component (mean of the data). This normalization procedure is crucial for compensating for non-uniform x-ray intensity or signal gain across the bar pattern.

### **Detective Quantum Efficiency**

Detective quantum efficiency (DQE) is measured as a function of the spatial frequency and used to characterize the capability of an imaging system to preserve the signal-to-noise ratio (SNR) in the input image signals. DQE is generally defined as follows:

$$DQE = \frac{SNR_{out}^2}{SNR_{in}^2}$$

where  $SNR_{in}$  and  $SNR_{out}$  are the image signal-to-noise ratios at the input and output. To measure the DQE as a function of the spatial frequency,  $f$  (lps/mm), we used the following expression for the frequency dependent DQE:

$$DQE(f) = \left( \frac{1}{SNR_{in}^2} \right) \cdot \left( \frac{S^2}{NPS(f)} \right) \cdot MTF(f)^2$$

where  $NPS(f)$  is the noise power spectrum,  $S$  is the average signal over the area where  $NPS(f)$  is measured,  $MTF(f)$  is the modulation transfer function. This equation is similar to those previously used in literature on DQE measurement<sup>8,9,11,15</sup>.

To compute the DQE(f), NPS(f) is computed from image data over an area with largely uniform signals while  $SNR_{in}$  is computed from the number of photons which is estimated from the x-ray techniques used.

### 3. Phantom Images

Image quality of a mammographic unit is often checked with phantoms simulating a breast with the three major disease symptoms: microcalcifications and masses. Various phantoms have been designed for this purpose. We have used two commercial phantoms to test the image quality and compare different imaging systems or technical factors. The first one is a Tissue-Equivalent Breast Phantom made by the Computerized Imaging Reference Systems (CIRS), Inc. of Norfolk, Virginia. It consists of a breast shape phantom made of tissue equivalent material, with a step wedge, groups of microcalcifications, masses and fibrils embedded inside the phantom. A specification sheet for the phantom is attached as Appendix II. The step wedge consists a square region with a contrast corresponding to additional 5mm of glandular tissue over the surrounding background tissue and a second square region with a contrast corresponding to additional 5mm of fat tissue. The 12 microcalcification groups ranges from 0.12mm to 0.35mm in diameter. The 6 masses range from 1mm to 6mm in diameter. The fibrils have a diameter of  $8.7\mu\text{m}$ . This phantom provides a good tool for comparing the overall image quality of different imaging systems, techniques or technical factors.

The second phantom is the RMI Anthropomorphic Breast Phantom (Model 165, Gammex-RMI). The phantom consists of a breast tissue equivalent (50% adipose, 50% glandular) plastic casting and a high resolution detail layer enclosed in a protective acrylic case. Together, these components produce radiographic images that are similar to a true mammogram.. To aid the evaluation of system performance, the phantom also produces a nine level gray scale step wedge and a group of resolution line pairs in the mammogram. The phantom is unique in that the characteristics of its components were derived from an actual mammogram. The three dimensional surface structure of the breast tissue equivalent plastic casting produces the low and medium resolution image detail. High resolution image details are produced by an attenuating coating of a stable

mercury-silver amalgam on photographic film. In addition to protecting the contents, the acrylic case acts as a uniform attenuation layer across the entire phantom

The advantage of using the above two phantoms is that they more or less simulate a real breast in tissue thickness, composition and even structures. Thus they allow performance check in realistic imaging situation. However, they are more suitable for quality control than for critical comparison of image quality. The simulated microcalcifications in the CIRS phantom have a size of at least 120 $\mu$ m. In addition, the sizes of different groups increment by 40 $\mu$ m. To facilitate more critical and quantitative comparison of image quality, we have developed a phantom referred to as the aluminum wire phantom (AWP). The AWP is constructed of aluminum wires of 8 different sizes: 2, 3, 4, 5, 6, 7, 8 and 16 mils. These wires were cut into about 1" long and placed in radial directions over a 1" thick Lucite block. A group of five short wire segments, cut from the size of wire, are placed near the tip of each wire. This phantom allows subtle difference between different imaging systems or techniques to be studied.

For comparison study or quality control, these phantoms are normally imaged with X-ray techniques often used with screen-film combinations in clinical studies. These factors were generally determined by setting the kVp desired and then exposing a Min-R screen-film cassette in the automatic exposure (mAs) mode. The film was then processed and the resulting film image examined to check the density of the image. The kVp and mAs are recorded and used for storage phosphor imaging if the film density appear to be adequate. For the CIRS phantom, the proper techniques for the Min-R screen-film combination are 208 mAs at 25 kVp with an antiscatter used. For the aluminum wire phantom, the techniques are usually set at 25 kVp and 26 mAs with grids.

#### **4. Image Acquisition for ROC Study**

In the proposed project, we will conduct a ROC study to compare the improved storage phosphor imaging technique with the conventional screen-film technique. The study will be based on phantom images with simulated tissue structures, microcalcifications, and masses. To present more realistic imaging conditions, these objects will be superimposed with structures mimicking tissue structures of breasts. In the second year, we have finalized our design and constructed a phantom for generating images for the ROC studies. Actual image acquisition using this phantom has started and is expected to be completed in January of 1995. Methods for phantom construction and image acquisition will be described and discussed in this section.

#### **Phantom Construction**

The main body of the phantom is supposed to provide a background structure over which microcalcifications and masses will be simulated and superimposed. We have investigated several approaches to construct the main body of the phantom. The final design is a large 1" thick piece of beef housed in a specifically designed plastic tank. This design is intended to simulate a well compressed breast. The meat produces a structural

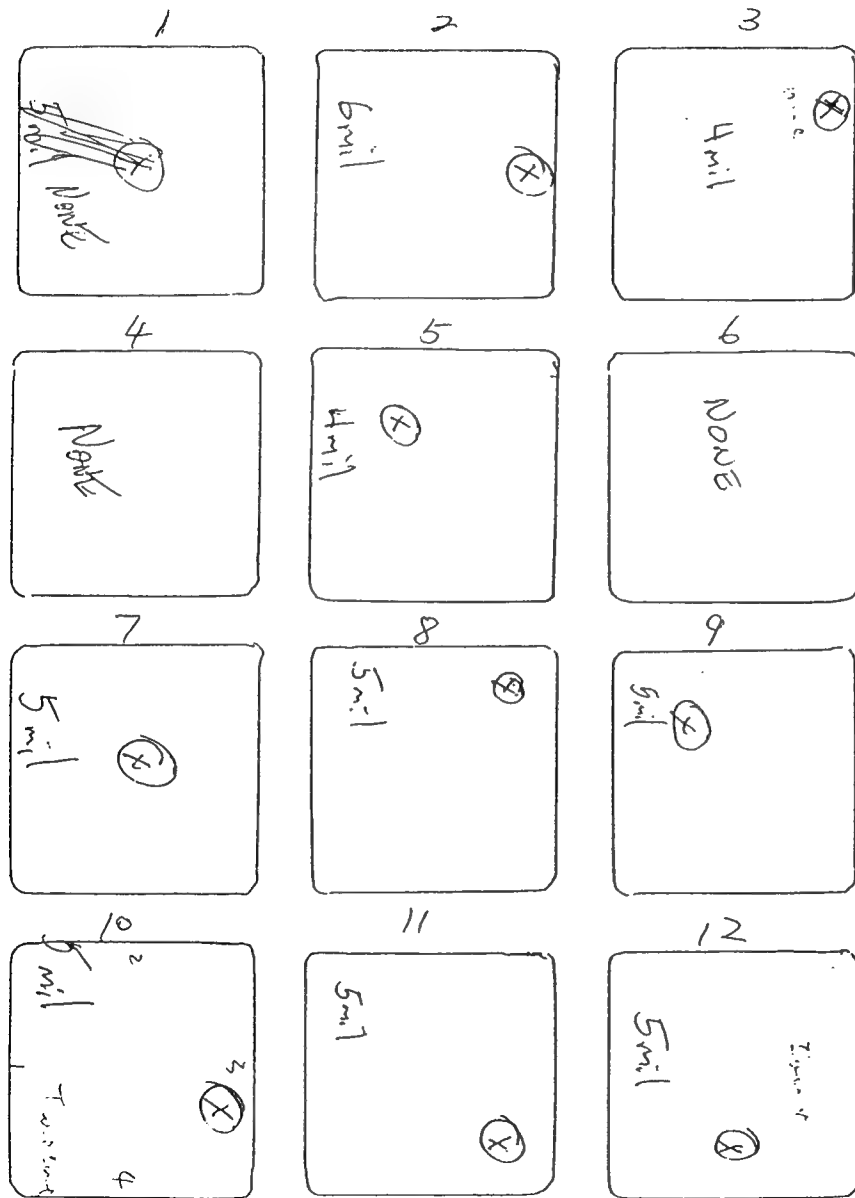


Figure 1 Layout of the film holder for the meat phantom used to acquire images for the ROC study. A matrix of 3x4 1.5"x1.5" film inserts can be placed on the holder to provide 12 independent reading tasks. Examples of the microcalcification placement are shown in the windows #2,3,5,7,8,9,10,11,12.

pattern different from real mammograms but still provides adequate challenge to the tasks of detecting simulated microcalcifications or masses. The meat can be easily replaced to produce a different structural background so that the reader has no opportunity to become "trained" for a certain pattern. The tank is filled with pure alcohol to preserve the meat for longer time. The thickness of the tank is minimized to about 0.5". Thus, the phantom has a total thickness of 1.5".

Mircocalcifications (MC) are simulated by a group of 5 or 6 aluminum wire segments (spread over an area of 2-3 mm wide) placed on a 1.5"x1.5" piece of plastic film (cut from acetone transparency). The MCs are simulated with three different sizes: 4, 5 and 6 mils(100, 125 and 150 $\mu$ m). Other sizes weren't used because visual tests have indicated that MCs larger than 6 mil are always visible while those smaller than 4 mil can never be seen under clinical imaging conditions. For each size, many film pieces were made with the MCs located at various locations. These films can also be rotated by multiples of 90 degrees to further randomize the location of the MC groups. Films without any MC were also made to simulate normal cases. A film holder is constructed of a 3/8" thick piece of Lucite with a 3x4 matrix of 1.5"x1.5" holes cut out. During image acquisition, the holder, with 12 selected film inserts, is placed underneath the meat phantom for exposure. Figure 1 shows the layout of these cutouts. Films 8 and 9 show examples of the x-ray images of the meat phantom with simulated MCs.

Statistical analysis in the proposal has indicated that 240 observations (readings) are required to yield reasonable significance of the ROC study. Our phantom design provides 12 "windows". Within each of these windows, an observation or reading can be performed to determine whether and where there are MCs. Thus, each image will provide 12 independent readings and a total of 20 different images will be required. A total of 240 inserts are required to acquire these 20 images (12 for each of them). Among the 240 film inserts used, 40 have no MCs, 40 have 6 mil MCs, 80 have 5 mil MCs and 80 have 4 mil MCs. These inserts are randomly selected by a computer program to be used in each image acquisition procedure.

The masses are simulated by circular cutout of tape attached to the film insert. The size and thickness of the wax drops can be varied to simulate masses different sizes and contrast. To produce marginal visibility, hree different combinations of thickness and size will be simulated and studied: (A) 2mm wide double tape, (B) 2mm wide single tape and (C) 1mm single tape. 240 inserts containing simulated masses are used. Similar to the microcalcification study, 40 inserts have no mass, 40 have type A masses, 80 have type B masses and 80 have type C masses. Selection of film inserts for image acquisition is controlled and randomized by computer program.

### Image Acquisition

A clinical mammographic unit (LoRAD M-III) is used for image acquisition. The x-ray tube uses a molybdenum target. A 5:1 reciprocating antiscatter grid is used. With the phantom in place, a screen-film image is first taken using Kodak Min-R screen and

Min-R E film in the autotimed mode. The kVp is kept fixed at 25 kVp and the mAs is controlled by photo-timing. Following the exposure, the mAs will be recorded. The exposed film will then be developed and checked for proper exposure. If the film exposure is adequate, the storage phosphor cassette will be inserted and exposed using identical x-ray techniques. The exposed storage phosphor screen will then be scanned with a pixel size of 43 $\mu$ m to generate a 4096x5000x12 bit digital image. The image will first be printed with a 80 $\mu$ m pixel size using a Kodak Ektascan laser printer. The film will be examined and checked for any artifacts or phantom position. If acceptable, the phantom will be fitted with a different set of film inserts and imaged again following the same procedure.

### **Quality Control**

Quality control of the storage phosphor imaging system has been performed by acquiring and visually checking images of the resolution bar pattern, CIRS phantom, RMI phantom and the specially designed aluminum wire phantom. Because some improvements have been made on the system, the criteria for visual check has slightly changed now. In general, for the resolution bar pattern image, we expect to see and resolve all bars at frequencies of up to 8.5 lps/mm fully and clearly. The 10 lps/mm bars should also be fully resolved but with subdued contrast. Partially resolution of the 10 lps/mm bars is an indication of presence of structural artifacts. The images of the CIRS phantom provides a convenient semi-quantitative method for checking the overall quality of the system, including the spatial resolution and noise properties. Same technique (25kVp, 208mAs, 65cm SID, with antiscatter grids) will be used in all quality control exposures. In general, we expect to see all microcalcifications with a diameter of 200 $\mu$ m or greater and all masses with a diameter of 2mm or greater. All fibrils should be fully resolved. The RMI phantom offers a more qualitative check. All images should have similar apparent quality as previous images. The aluminum wire phantom provides a finer technique to grade the system performance. At 25 kVp and 26 mAs, we expect to resolve the 1" long wires as thin as 50 $\mu$ m in diameter and small wire segments as thin as 125 $\mu$ m.

Quality control of mammographic X-ray units and the screen-film combinations have been previously discussed<sup>110,111</sup>. The quality of the mammographic X-ray unit is routinely monitored and maintained by the clinical staff.

### **5. Image Data Compression**

The data compression procedure is divided into two parts: preprocessing and Joint Photographic Experts Group (JPEG) compression. They are summarized in this section. A detailed description and discussion of the methods are presented in the manuscript reprint attached as Appendix V.

### **Preprocessing**

Before applying the JPEG compression algorithm, the image data is preprocessed to improve its compressibility. This preprocessing operation is divided into two phases; first the image is segmented and cropped and the background pixel values are modified to minimize the storage requirements for the background. We begin the segmentation process by automatically determining a threshold value from the histogram of the digitized source image that indicates the transition between background values and tissue values. This threshold value is used to classify pixels in the image as either tissue or background so as to produce a two-valued mask corresponding to the tissue-background separation.

The second phase of preprocessing involves the application of a noise-removal filter to the tissue area of the image. The particular filter tested here is a nonlinear order filter that was designed to modify mainly pixels with large noise components while leaving the majority of pixels unchanged.

### **JPEG Compression**

The JPEG compression algorithm used in this study is a software package written and tested in our laboratory that implements the 12-bit version of the extended JPEG standard. For this study, Huffman encoding was used to encode the quantized coefficients and all compression ratios were based on this. The Huffman tables were derived from the statistics of each individual quantized image rather than on the ensemble statistics. Signaling information was not included in the code size when calculating compression ratios.

### **Evaluation**

The compression technique is evaluated by its speed, compression ratio and ability to preserve image information. Measurement of the compression and decompression speed is straightforward. The results, however, are dependent upon individual images. Therefore, we evaluated and compared the average speeds for the 8 images used in our study.

The purpose of preprocessing is to increase the information content in the image. Thus, we measured the average number of bits for each 8x8 pixel block of tissue area before and after segmentation. An improvement factor is computed as the ratio of average number of bits before the segmentation to that after the segmentation. We also measured the percentage of image area with breast tissue signals.

The compression ratio and ability for information preservation are not independent of each other. It is reasonable to expect better information preservation when the compression ratio is low and vice versa. We used a just noticeable difference (JND) study to quantify the information preservation as a function of the compression

ratio. From eight original mammograms, which had each been compressed at five compression ratios, a set of 40 randomized pairs of images, each consisting of one laser printed non-compressed image and one compressed image were assembled. 20 readers were asked to view the pairs side by side and forced to choose the compressed image. The readers include experienced radiologists, physicists and engineers specializing in medical imaging. Following the study, the results are sorted according the compression ratio and the percentage of corrected selected pairs is plotted as a function of the compression ratio for a group of "expert readers" and a group of "average readers".

## RESULTS AND DISCUSSION

### 1. Spatial Resolution Comparison

Film 1 shows a storage phosphor image of a resolution test pattern (Nuclear Associates, Model 07-553) acquired with a high resolution storage phosphor screen and scanned with the modified storage phosphor image reader with a reduced beam spot size of 40 $\mu$ m and a pixel size of 43 $\mu$ m. Notice that the 10 lps/mm bars are clearly rendered. The horizontal resolution is slightly better than the vertical one. Film 2 shows a storage phosphor image of the resolution test pattern acquired with a 14"x17" standard resolution storage phosphor screen and scanned with a commercial storage phosphor image reader (KESPR, Eastman Kodak Company). The pixel size is 173 $\mu$ m. Notice that bar pattern is resolved at up to 2.4 lps/mm. Although there is ample contrast, serious aliasing effects are present at frequencies above 2.4 lps/mm. Film 3 shows a storage phosphor image of the resolution test pattern acquired with a 8"x10" high resolution storage phosphor screen (Fuji HRIIIn) and scanned with a commercial storage phosphor image reader (KESPR, Eastman Kodak Company). The pixel size is 100 $\mu$ m. Notice that bar pattern is resolved at up to 5 lps/mm. Although there is some contrast, serious aliasing effects are present at frequencies above 5 lps/mm.

These images demonstrate that our improved ESPIS results in much better spatial resolution than those obtained with commercial storage phosphor imaging systems. We have also measured and compared the MTFs for the above three different imaging systems. The results are shown in Figure 2. The comparison of the MTFs also show that our improved ESPIS results in much better spatial resolution properties. The poorer spatial resolution of the tested commercial systems is due to two factors: the large sampling size and large laser beam spot size. The bar pattern image in Film 1 has shown some improvement when compared to those obtained in 1993 (see 1993 report). The improvement may be attributed to finer focusing and a reduction of the laser spot size from 50 $\mu$ m to 40 $\mu$ m. The MTF measured for the improved ESPIS is comparable to other digital mammography techniques based on a combination of x-ray conversion and light detection methods. This is probably due to the fact that image blurring from light diffusion in x-ray phosphors sets a fundamental limit on the MTFs of all this category of systems, including our ESPIS.

We have also measured the MTF as a function of the laser beam power, ranging from 8 to 12 mW. The results, shown in Figure 3, indicate that there is no dependence on the laser beam power in the useful range of 8-12 mW. It should be noted that outside this range, the power may be too strong to avoid overheating or even burning the phosphor or it may be too low for the position encoding to properly function.

### 2. Detective Quantum Efficiency (DQE)

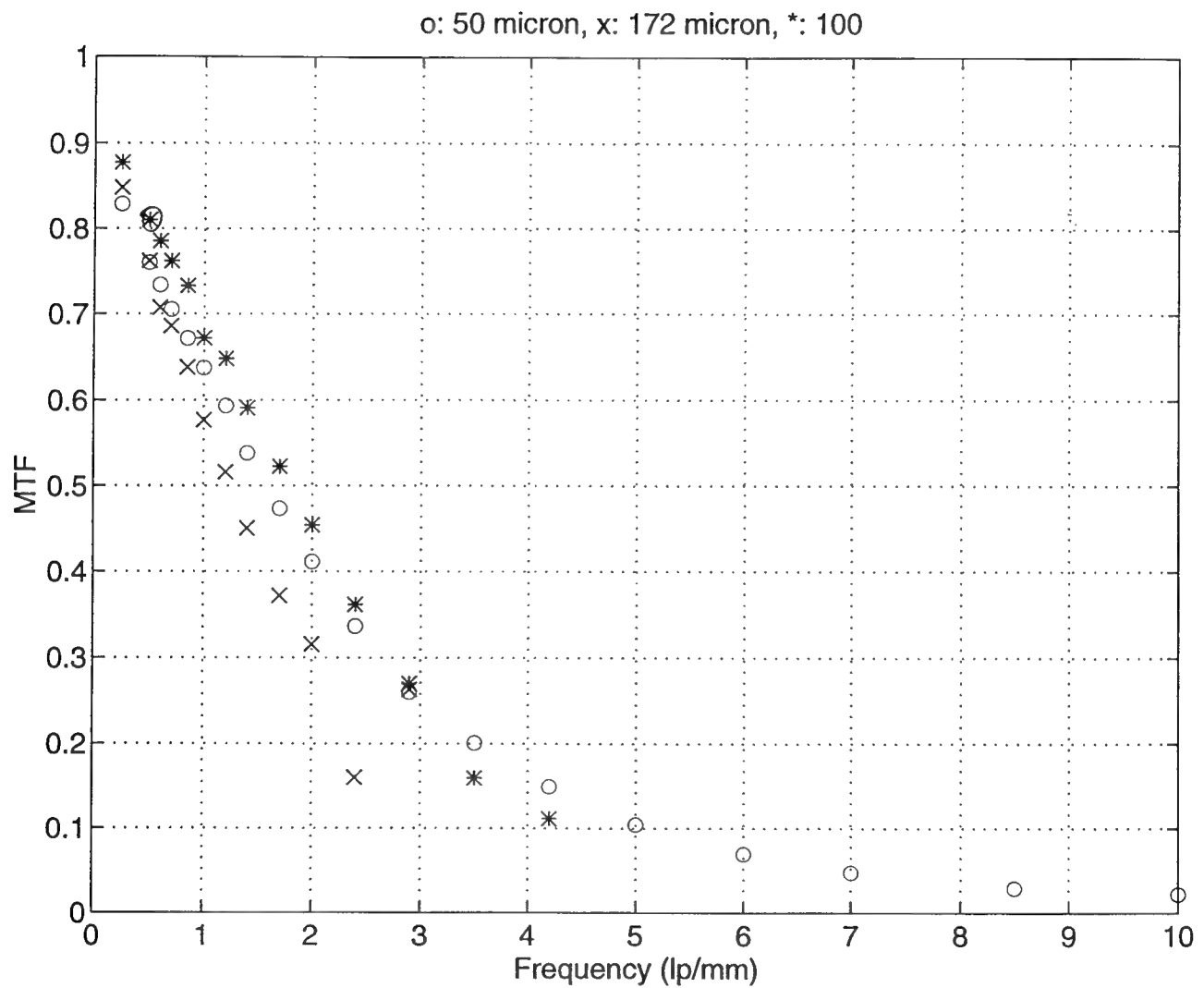


Figure 2 MTFs for three different storage phosphor imaging systems: "o": Fuji HR III In screen scanned by an experimental storage phosphor image reader with a pixel size of 43  $\mu$ m and a spot size of 40  $\mu$ m, "\*": Kodak standard resolution screen scanned by KESPR with a pixel size of 173  $\mu$ m, and "o": Fuji HR III In screen scanned by KESPR with a pixel size of 100  $\mu$ m. The spot size for KESPR is estimated to be between 120 and 200  $\mu$ m.

MTF of FJ plates, LP: 8(\*), 10(+) 12(x)and 16(o) images

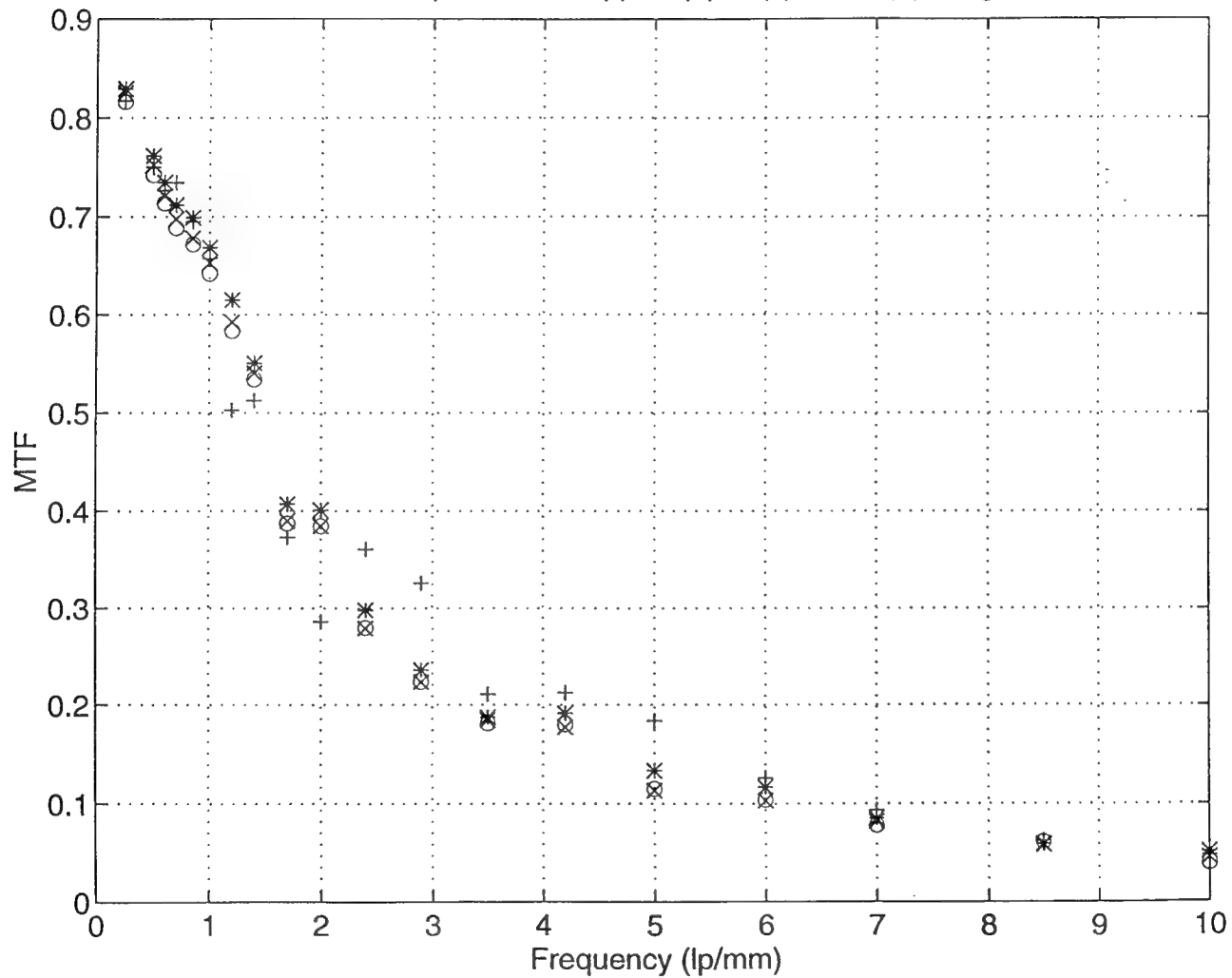


Figure 3 Effect of laser power on the MTF. The MTF was measured for various laser powers, ranging from 8 to 16 mW: "\*": 8 mW, "+": 10 mW, "x": 12 mW and "o": 16 mW.

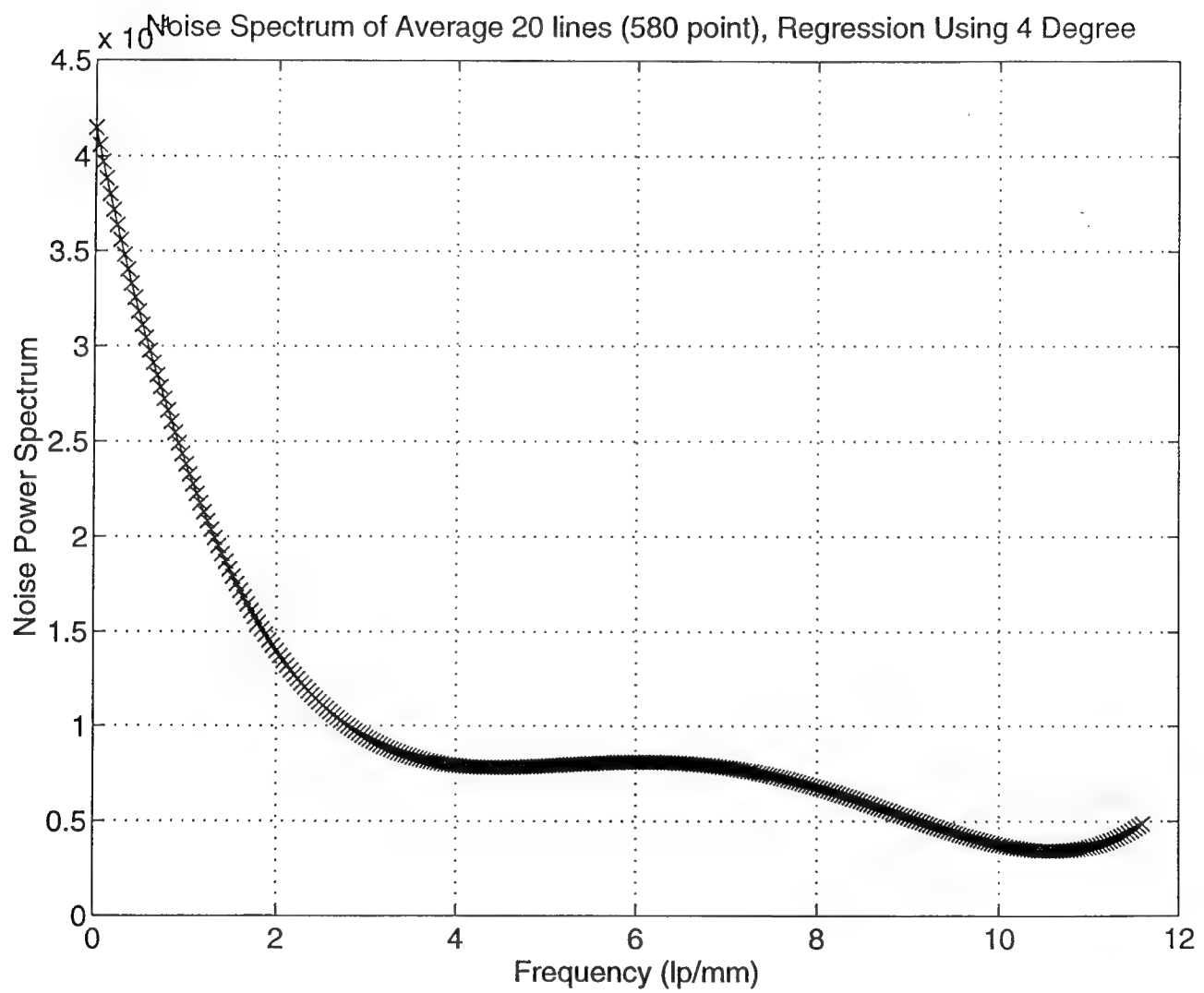


Figure 4 Noise power spectrum computed from image data in an area of largely uniform brightness. The spectrum was normalized by dividing it by the square of the average signal.

DQE of Average 20 lines (580 point)

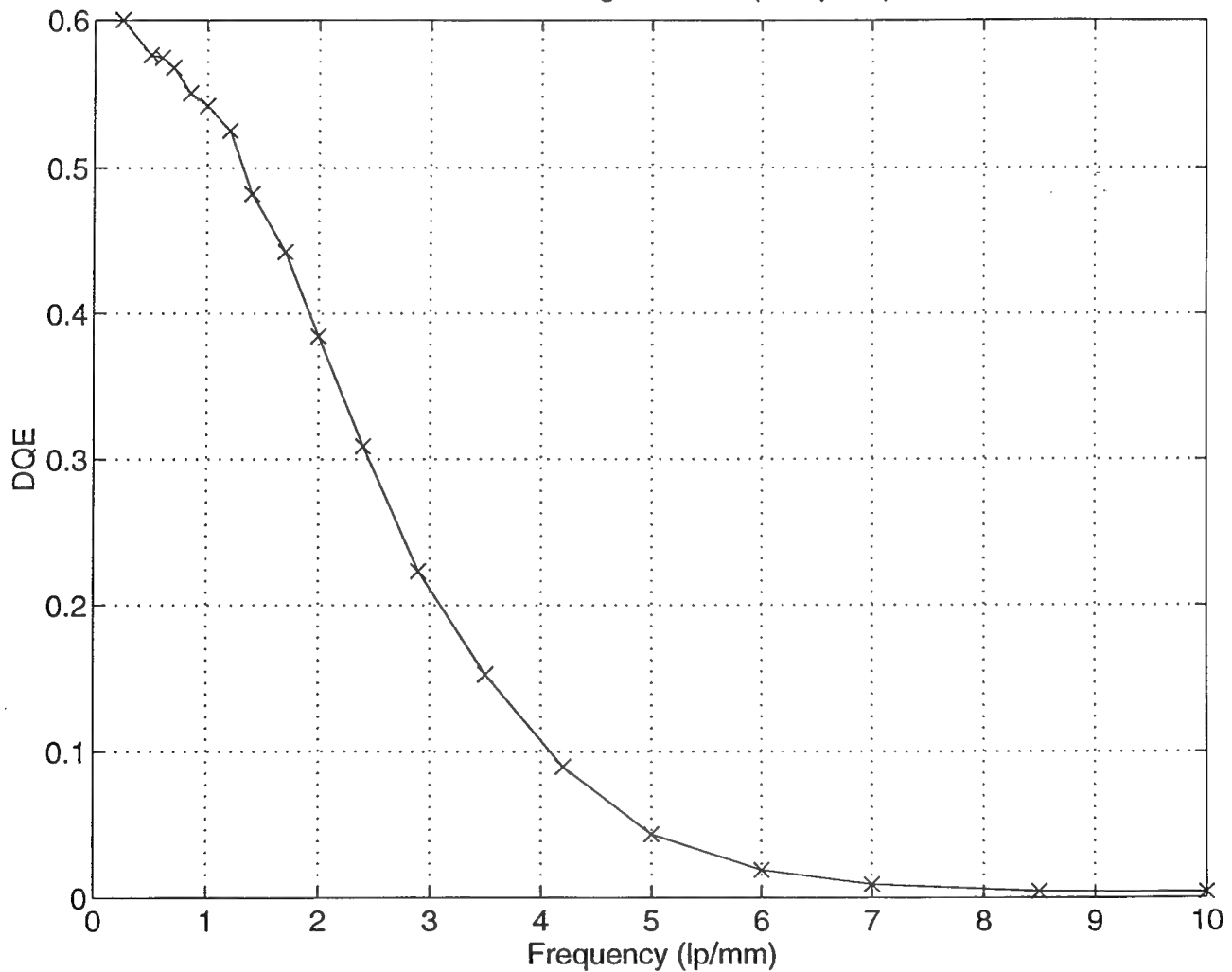


Figure 5 DQE versus spatial frequency for the improved experimental storage phosphor imaging system.

We have measured the noise power spectrum (NPS) and detective quantum efficiency (DQE) for our ESPIS. Figure 4 shows the noise power spectrum computed from the image data in a largely uniform region. The x-ray techniques used in acquiring the image data are 25 kVp, 10 mAs, with grids at an SID of 65 cm. The resulting detector exposure is approximately 6 mR. Notice that because of image blurring, the noise spectrum is no longer white. Instead, it decreases with increasing frequency. Figure 5 shows the DQE plotted as a function of the frequency. We are currently refining our technique for the DQE measurement. We are also trying to compare our results with those done at other institutions.

### 3. Phantom Images for Performance Comparison

To check the image quality following the improvement of the ESPIS, we have acquired images with a CIRS phantom and a specially designed aluminum wire phantom. Film 4 shows a storage phosphor image of a CIRS breast phantom acquired with a high resolution storage phosphor screen (Fuji HR3In) and scanned with the improved ESPIS. The x-ray techniques used are identical to those used in obtaining the screen-film image in Film 5. Notice that most calcifications (with a diameter of 8 mils or greater) and masses (with a diameter of 2 mm or greater) are well resolved. It should be noted that compared to images obtained in 1993 (see 1993 report) the ESPIS still can not resolve the 160 $\mu$ m or smaller MCs or 1 mm mass. However, it does resolve the 200 $\mu$ m MCs and 1mm mass in a much more clear way, indicating that the ESPIS has been improved somewhat.

Film 5 shows a screen-film image of the specially designed wire phantom acquired with grids at 25 kVp and 208 mAs. The screen-film image shows the calcifications, masses and fabrils with a sharper appearance which is partially due to its smaller (by a factor of 2) format. However, it does not resolve more than what can be resolved in the storage phosphor image. This shows that at typical clinical exposure level (as determined by the automatic exposure control), the improved storage phosphor imaging system approaches the conventional screen-film combinations in quality as far as detection of microcalcifications and masses is concerned.

Film 6 shows a storage phosphor image of the specially designed wire phantom acquired with a high resolution storage phosphor screen (Fuji HR3In) and scanned with the improved storage phosphor image reader. The x-ray techniques used are identical to those used in obtaining the screen-film image in Film 7. Notice that the 5 mil (125 $\mu$ m) wire segments are well resolved while the 4 mil (100 $\mu$ m) wire segments are only marginally resolved. All but the 2 mil (50  $\mu$ m) long wires (oriented in radial direction) are resolved.

Film 7 Screen-film image of the specially designed wire phantom acquired with grids at 25 kVp and 26 mAs. The screen-film image shows the wire segments with a sharper appearance which is partially due to its smaller (by a factor of 2) format. This helps resolve the 4 mil (100 $\mu$ m) wire segments. However, it does not resolve finer

segments (2, 3 mil) or wires (2 mil). This shows that at typical clinical exposure level (as determined by the automatic exposure control), the improved storage phosphor imaging system approaches the conventional screen-film combinations in quality as far as detection of microcalcifications is concerned.

#### **4. Phantom Images for ROC Study**

We have designed a phantom for acquiring images for use in the ROC study. As described in the Methods section, the phantom allows the structural background as well as simulated MCs or masses to be changed. We are currently in the process of acquiring the images for the ROC study. An example set of images are presented and discussed in this section.

Film 8 shows a storage phosphor image of the multiple window meat phantom designed for image acquisition in this project. Groups of five calcifications (simulated by 4, 5 or 6 mil aluminum wire segments) are present in selected window #2, 3, 5, 7, 8, 9, 10, 11 and 12. 5 and 6 mil calcifications are largely visible with different degrees of difficulty, depending on the background structures. 4 mil calcification are generally difficult or impossible to visualize.

Film 9 shows a screen-film (Min-R screen and Min-R E film) image of the multiple window meat phantom designed for image acquisition in this project. Notice that the aluminum wire segments (to simulate calcifications) have a sharper appearance in the screen-film image. This increases the ease for the 5 and 6 mil calcifications to be seen. However, 4 mil calcifications (in window #3 and 5) are still difficult to detect though perhaps not impossible.

Although the final comparison of our ESPIS with the conventional screen-film combination awaits the results of the ROC study. From the images we have seen, it appears that the quality of the ESPIS approaches that of screen-film systems when imaging MCs over uniform background. However, the sharper appearance of the screen-film images makes the task of detecting the MCs significantly easier. As the result, detecting 4 or 5 mil MCs in the screen-film images may have a higher success rate.

#### **5. Data Compression**

We will summarize our results from the data compression study in regard to three topics: speed of our compression system, performance of preprocessing and performance of the JPEG compression. A manuscript is attached as Appendix V for a more detailed description and discussion of the results.

### **Speed**

The speed of our compression system is somewhat image dependent. It averages about 20 s/Mbyte to preprocess and compress source data. Decompression is faster at 15 s/Mbyte because there is no preprocessing involved. These speeds may not be acceptable for clinical use with a picture archival and communication system (PACS). However, they can be easily improved by using dedicated and optimized hardware as much as possible.

### **Preprocessing**

A summary of the effect of image segmentation on the number of bits needed to represent tissue blocks is shown in Table 1 in which the percentage of image area containing tissue signals, bits per tissue block before and after segmentation, and the improvement factor are listed for each of the 8 original mammograms. From these results, the information content of the image has been improved by a factor of 2.7 on the average despite the fact that the background only represented 36% of the image area.

### **JPEG Compression**

In Figure 6, the performance of image processing specialists and nonspecialists, measured by the ratio of correct identification of compressed images, is plotted as a function of the compression ratio. These results verify our expectation that the higher the compression ratio is, the more information change there is and therefore the easier one can identify the compressed images. However, the impact of data compression on diagnostic accuracy must be evaluated by a ROC study.

**Table 1: The Effect of Image Segmentation on Tissue Block Representation (bits per block)**

Image	% of Area Representing Tissue	Bits per Tissue Block (no preprocessing)	Bits per Tissue Block (after segmentation)	Improvement Factor
1	51.1	8.6	30.1	3.5
2	52.9	8.5	27.0	3.2
3	70.5	9.1	32.3	3.5
4	71.7	10.0	28.0	2.8
5	72.4	9.4	23.6	2.5
6	56.8	7.6	26.5	3.5
7	70.7	24.2	27.4	1.1
8	67.0	18.0	22.2	1.2

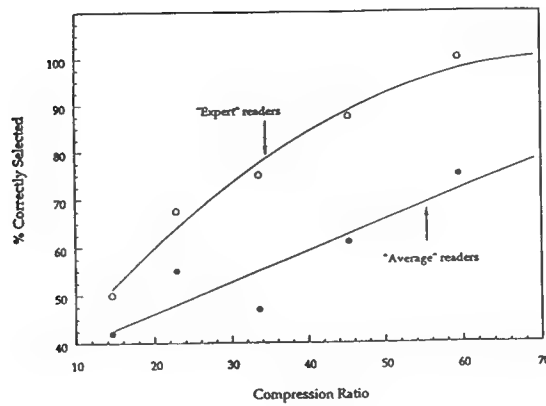


**Fig 6. Performance of image-processing specialists and nonspecialists for the task of identifying compressed versus noncompressed images.**

## CONCLUSIONS

In the second year of the grant period, we have completed the following tasks:

1. We have improved the spatial resolution capability of our storage phosphor image reader by further reducing the laser spot size from  $50\mu\text{m}$  (obtained in first year) to  $40\mu\text{m}$ .
2. We have measured and compared the MTFs of the improved system with those of commercial systems.
3. We have developed a phantom for monitoring the overall image quality.
4. We have constructed and tested phantoms for the comparison study.
5. We have begun acquisition of storage phosphor and film images for the ROC study.
6. We have completed the test of the compression algorithms developed in the previous year.

We have demonstrated with phantom images that the quality of the storage phosphor images, obtained with the improved imaging system, are superior to those obtained with current commercial systems. We have also shown that the quality approaches that of the screen-film images. We anticipate that image acquisition will be completed in January of 1995 and the ROC study will begin in February.

## REFERENCES\*

1. Fuhrman CR, Gur D, Good BC, et al. The diagnostic quality of storage phosphor radiographs compared to conventional films: interpreter's perception. *AJR* 1988; 150:1011-14.
2. Fuhrman CR, Gur D, Schaetzing R. High resolution digital imaging with storage phosphors. *J Thoracic imaging* 1990; 5:12-30.
3. Gur D, Deutsch M, Fuhrman CR, et al. The use of storage phosphors for portal imaging in radiation therapy: therapists's perception of image quality. *Med Phys* 1989; 16(1):132-6.
4. Weiser JC, Gur D, Cano E, Deutsch M, Wu A, Mogus R. Verification of electron beam therapy with storage phosphor images: precision of field placement. *Radiol* 1990; 175:257-259.
5. Slasky BS, Gur D, Good WF, Costa-Greco MA, Harris KM, Cooperstein LA, Rockette HE. Receiver operating characteristic analysis of chest image interpretation with conventional, laser-printed, and high-resolution workstation images. *Radiol* 1990; 174:775-780.
6. Rosenthal MS, Good WF, Costa-Greco MA, Miketic LM, Eelkema EA, Gur D, Rockette HE. The effect of image processing on chest radiograph interpretations in a PACS implementations in a PACS environment. *Invest Radiol* 1990; 25:897-901.
7. Schaetzing R, Whiting BR, Lubinsky AR, Owen JF. Digital radiography using storage phosphors. in *Digital imaging in diagnostic radiology*, published by Churchill Livingstone (1989).
8. Hillen W, Schievel U, Zaengel T. Imaging performance of a digital storage phosphor system. *Med Phys* 1987;14:744.
9. Fujita H, Ueda K, Morishita J, Fujikawa T, Ohtsuka A, Sai T. Basic imaging properties of a computed radiographic system with photostimulable phosphors. *Med Phys* 1989;16(1):338-345.
10. Lubinsky AR, Owen JF, Korn DM. Storage phosphor system for computed radiography: screen optics. *SPIE* 1986;626:120-132.
11. Lubinsky AR, Whiting BR, Owen JF. Storage phosphor system for computed radiography: optical effects and detective quantum efficiency (DQE). *SPIE* 1987;767:167-177.
12. Fujita H, Ueda K, Ohtsuka A. Resolution property of digital radiography with photostimulable phosphors. I. Measurements of imaging plate MTF's. *Jpn J Med Imag Inform Sooc* 1987; 4:89.
13. Fujita H, Ueda K, Fujikawa, Ohtsuka A. Resolution property of digital radiography with photostimulable phosphors. II. Measurements of digital characteristic curve and presampling MTF. *Jpn J Med Imag Inform Sooc* 1988; 5:1.
14. Shaw CC, Herron JM, Gur D. Signal fading, erasure and rescan in storage phosphor imaging. *SPIE* 1992;1651 *Image Physics*. In press.
15. Bunch PC. Dectective quantum efficiency of selected mammographic screen-film combinations. *Proc SPIE* 1989; 1090:67-77.
16. Silverberg E, Lubera JA: A Review of American Cancer Society estimates of cancer cases and deaths. *CA* 1983; 33:2-8.
17. Silverberg E: *Cancer statistics, 1983*. *Ca* 1983; 33:9-25.
18. Nathan S: *An Atlas of Normal and Abnormal Mammograms*. Oxford; New York; Oxford University Press, 1982.

19. Feig SA, McLelland R, Eds: *Breast Carcinoma: Current Diagnosis and Treatment*. New York, Masson Publishing USA, Inc, and the American College of Radiology, Chicago, 1983.
20. National Task Force on Breast Cancer Control: *Mammography: A statement of the American Cancer Society*. Conn Med 1983; 47:37-9.
21. Moskowitz M, Gartside PS: Evidence of breast cancer mortality reduction: Aggressive screening in women under age 50. AJR 1982; 138:911-6.
22. Venet L, Shapiro S, Strax P, Venet W: Effect of screening on survivals. In: *Early Breast Cancer/Detection and Treatment*, New York, John Wiley & Sons, 1975.
23. Pavlov KA, Semiglazov VF: Detection of early forms of breast cancer by mass screening examinations. *Neoplasma* 1981; 28:611-5.
24. *Breast Cancer Digest* 1979; 80:1691.
25. Strax P: Control of breast cancer through mass screening. *JAMA* 1976; 235:1600-2.
26. Thomas BA, Price JL, Boulter PS. Breast cancer population screening by single view mammography with selective clinical examination--A pilot study. *Clin Oncol* 1981; 7:201-4.
27. Tabar L, Gad A: Screening for breast cancer: The Swedish trial. *Radiology* 1981; 138:219-22.
28. Andersson I, Andren L, Hildell J, Linell F, Ljungqvist U, Pettersson H: Breast cancer screening with mammography. *Radiology* 1979;273-6.
29. Beahrs OH, Shapiro S, Smart C: Report of the working group to review the NCI/ACS breast cancer detection demonstration projects. NCI 1977.
30. Beahrs OH, Shapiro S, Smart CH, et al: Report of working group to review BCDDP. *J Natl Cancer Inst* 1979; 62:679-90.
31. Strax P: Organization of mass screening programs in breast cancer--Including identification of high-risk groups. In: *Early Diagnosis of Breast Cancer*, Grundman E, Beck L, Eds. Stuttgart, Gustav Fischer Verlag, 1978.
32. Lundgren B, Helleberg A: Single oblique-view mammography for periodic screening for breast cancer in women. *JNCI* 1982; 68:351-5.
33. Haus AG: Physical principles and radiation dose in mammography. *Med Radiogr Photogr* 1982; 58:70-80.
34. Moskowitz M, Gartside PS, Gardella L, deGroot I, Guenther D: The breast cancer screening controversy: A perspective. In: *Breast Carcinoma: The Radiologist's Expanded Role*. Logan WW, Ed. New York, John Wiley & Sons, 1977, pp 35-52.
35. Moskowitz M: Screening for breast cancer: How effective are our tests? A critical review. *CA* 1983; 33:26-39.
36. Moskowitz M: Mammographic screening: Significance of minimal breast cancers. *AJR* 1981; 136:735-8.
37. Leborgne RA: *The Breast in Roentgen Diagnosis*. London, Constable and Co., 1953.
38. Ingleby H, Gershon-Cohen J: *Comparative Anatomy, Pathology and Roentgenology of the Breast*. Philadelphia, University of Pennsylvania Press, 1960.
39. Stanton L, Villafana T, Day JL, Lightfoot DA: A breast phantom method for evaluating mammography technique. *Invest Radiol* 1978; 13:291-7.
40. Miller DW: Center for Radiological Physics: Mammography Review Procedures and Results. In: *Breast Carcinoma: The Radiologist's Expanded Role*. Logan WW, Ed. New York, John Wiley & Sons, 1977, pp 129-33.
41. Porrath SA: XERG mammography: A review of sixteen months experience plus a comparison with xeromammography. In: Logan W, Muntz EP, *Reduced Dose Mammography*. New York, Masson Publishing USA, 1979, pp 389-94.

42. Hirschfeld RL: XERG and lo-dose mammography: A comparative clinical study. In: Logan WW, Muntz EP: Reduced Dose Mammography. New York, Masson Publishing USA, 1979, pp 395-405.

43. Sickles EA: Heavy-particle mammography. In: Breast Carcinoma: The Radiologist's Expanded Role. Logan WW, Ed. New York, John Wiley & Sons, 1977, pp 239-41.

44. Isard HJ: General discussion: Thermography in the mass screening of cancer. Ann NY Acad Sci 1980; 335:520-3.

45. Milbrath JR: Does thermography aid in breast cancer detection? In: Breast Carcinoma: The Radiologist's Expanded Role. Logan WW, Ed. New York, John Wiley & Sons, 1977, pp 255-8.

46. Chang CHJ, Sibala JL, Fritz SL, Dwyer SJ III, Templeton AW: Specific value of computed tomographic breast scanner (CT/M) in diagnosis of breast diseases. Radiology 1979; 132:647-52.

47. Gisvold JJ, Karsell PR, Reese DF: Computerized tomographic mammography. In: Breast Carcinoma: The Radiologist's Expanded Role. Logan WW, Ed. New York, John Wiley & Sons, 1977, pp 219-38.

48. Bryan RN, Hazelwood CF, Ford JJ, Fisher PB, Schneiders NJ, Garnil E: In vivo NMR imaging of the human breast. Presented at the 69th Annual Meeting of the Radiological Society of North America, Chicago, 1983.

49. Sickles EA, Davis PL, Crooks LE: NMR characteristics of benign and malignant breast tissues: Preliminary report. Presented at the 69th Annual Meeting of the Radiological Society of North America, Chicago, November 1983.

50. El-Yousef SJ, O'Connell DM, Duchesneau RH, et al. Radiofrequency pulse sequences for characterization of benign and malignant conditions of the breast. Radiology 1984; 153:52.

51. Cole-Beuglet C, Baltarowich O, Pasto ME, Rifkin MD, Kurtz AB, Goldberg BB: Ultrasound appearance of carcinoma in younger patients. Presented at the 69th Annual Meeting of the Radiological Society of North America, Chicago, November 1983.

52. McSweeney MB, Egan RL: Solid breast masses: Ultrasonographic, mammographic, and pathologic correlation. Presented at the 69th Annual Meeting of the Radiological Society of North America, Chicago, November 1983.

53. Muntz EP, Wilkinson E, George FW: Mammography at reduced doses: Present performance and future possibilities. AJR 1980; 134:741-7.

54. Jennings RJ, Eastgate RJ, Siedband MP, Ergun DL: Optimal x-ray spectra for screen-film mammography. Med Phys 1981; 8:629-39.

55. Brodie I, Gutcheck RA: Radiographic information theory: Correction for x-ray spectral distribution. Med Phys 1983; 10:293-300.

56. Barnes GT, Chakraborty DP: Radiographic mottle and patient exposure in mammography. Radiology 1982; 145:815-21.

57. Egan RL, McSweeney MB, Sprawls P: Grids in mammography. Radiology 1983; 146:359-62.

58. Barnes GT: Radiographic mottle: A comprehensive theory. Med Phys 1982; 9:956-67.

59. Zarand P, Pentek: Absorbed dose in "high filtration" xeromammography--An intercomparison. Radiol Diagn 1981; 22:240-6.

60. Sickles EA: Mammographic detectability of breast micro- calcifications. AJR 1982; 139:913-8.

61. Haus AG: Effect of geometric unsharpness in mammography and breast xeroradiography. In: Breast Carcinoma: The Radiologist's Expanded Role. Logan WW, Ed. New York, John Wiley & Sons, 1977, pp 93-108.

62. Brodie I, Gutcheck RA: Radiographic information theory and application to mammography. *Med Phys* 1982; 9:79-95.

63. Dodd GD: Radiation detection and diagnosis of breast cancer. *Cancer* 1981; 47:1766-9.

64. Hammerstein GR, Miller DW, White DR, Masterson ME, Woodard HQ, Laughlin JS: Absorbed radiation dose in mammography. *Radiology* 1979; 130:485-91.

65. Haus AG. Technologic improvements in screen-film mammography. *Radiology* 1990; 1174:628-37.

66. Haus AG. Recent trends in screen-film mammography: technical factors and radiation dose. *Recent Results Cancer Res* 1987; 105:37-51.

67. Haus AG. Recent advances in screen-film mammography. *Radiol Clin north Am* 1987; 25:913-28.

68. Sickles EA: Mammographic detectability of breast microcalcifications. *AJR* 1982; 139:913-8.

69. Muir BB, Lamb J, Anderson TJ, Kirkpatrick AE: Microcalcification and its relationship to cancer of the breast: Experience in a screening clinic. *Clin Radiol* 1983; 34:193-200.

70. Chan HP, Vyborny CJ, MacMahon H, Metz CE, Doi K, Sickles EA. Digital mammography: ROC studies of the effects of pixel size and unsharp-mask filtering on the detection of subtle microcalcifications. *Invest Radiol* 1987; 22:581-9.

71. Chan HP, Doi K, Galhotra S, Vyborny CJ, MacMahon H, Jokich PM. Image feature analysis and computer-aided diagnosis in digital radiography. I. Automated detection of microcalcifications in mammography. *Med Phys* 1987; 14:538-48.

72. Belikova TP, Yaroslavsky LP. Comments on "Image feature analysis and computer-aided diagnosis in digital radiography. I. Automated detection of microcalcifications in mammography." letter to *Med Phys* 1989; 16:142.

73. Chan HP, Doi K, Vyborny CJ, Schmidt RA, Metz CE, Lam KL, Ogura T, Wu Yz, MacMahon H. Improvement in radiologists' detection of clustered microcalcifications on mammograms: the potential of computer-aided diagnosis. *Invest Radiol* 1990; 25:1102-10.

74. Fam BW, Olson SL, Winter PF, Scholz FJ. Algorithm for the detection of fine clusttered calcifications on film mammograms. *Radiology* 1988; 169:333-7.

75. Dhawan AP, Le Royer E. Mammographic feature enhancement by computerized image processing. *Comput Methods Programs Biomed* 1988; 27:23-35.

76. Davies DH, Dance DR. Automatic computer detection of clustered calcifications in digital mammograms. *Phys Med Biol* 1990; 35:1111-8.

77. Fujita H, Ueda K, Ohtsuka A. Resolution property of digital radiography with photostimulable phosphors. I. Measurements of imaging plate MTF's. *Jpn J Med Imag Inform Sooc* 1987; 4:89.

78. Fujita H, Ueda K, Fujikawa, Ohtsuka A. Resolution property of digital radiography with photostimulable phosphors. II. Measurements of digital characteristic curve and presampling MTF. *Jpn J Med Imag Inform Sooc* 1988; 5:1.

79. Barnes GT, Sones RA, Tesic MM. Digital chest radiography: performance evaluation of a prototype unit. *Radiology* 1985; 154:801-806.

80. Doi K, Fujita H, Ohara K, et al. Digital radiographic imaging system with multiple slit scanning x-ray beam: preliminary report. *Radiology* 1986; 161:513-518.

81. Templeton AW, Dwyer III SJ, Cox GG, et al. A digital radiology imaging system: description and clinical evaluation. *AJR* 1987; 149:847-851.

82. Slasky BS, Sashin D, et al. Digital radiography of the chest by self-scanning linear diode arrays. *Acta Radop;gica* 1987; 28:461-466.

83. Fritz SL, Chang CH, Gupta NK, Martin NL, Laws RL, Anderson WH, Dwyer SJ, Templeton AW, Bernardi R, Fox T. A digital radiographic imaging system for mammography. *Invest Radiol* 1986; 21:581-3.
84. Rosenthal MS, Sashin D, Herron J, Maitz G, Boyer J, Gur D. Evaluation of a moving slit technique for mammography. *SPIE* 1991;1443 *Medical Imaging V-Image Physics*:132-142.
85. Nishikawa RM, Mawdsley GE, Fenster A, Yaffe MJ. Scanned-projection digital mammography. *Med Phys* 1987; 14:717-27.
86. Holdsworth DW, Gerson RK, Fenster A. A time-delay integration charge-coupled device camera for slot-scanned digital radiography. *Med Phys* 1990; 17:876-86.
87. Good WF. Bit allocation tables for the compression of chest images by JPEG type algorithms. *SPIE* 1992;1652 *Image Processing*. In press.
88. Photometrics. Charge-coupled devices for quantitative electronic imaging. 1991. Tuscon: Photometrics Ltd. 1-28.
89. Kennedy WH, Herron JM, Gur D, et al. X-ray imaging with two-dimensional CCD arrays. *Med Phys* 1985; 12(4):504.
90. Herron JM, Gur D, Daxon EG, Good WF, Shaw CC, et al. Digital x-ray imaging with two-dimensional charge-coupled device (CCD) arrays. *Proc SPIE* 1990; 1231:472-478.
91. Lawrence JL, Cope AD, Herron JM, et al. Medical x-ray imaging applications of the TEK2048 CCD. *Proc SPIE* 1990; 1242:59-65.
92. Kimme-Smith C, Bassett LW, Gold RH, Gormley L. Digital mammography: a comparison of two digitization methods. *Invest Radiol* 1989; 24:869-75.
93. Oestmann JW, Kopans D, Hall DA, McCarthy KA, Rubens JR, Greene R. A comparison of digitized storage phosphors and conventional mammography in the detection of malignant microcalcifications. *Invest Radiol* 1988; 23:725-8.
94. Kato Hisatoyo. Photostimulable phosphor radiography: design considerations. *Proc AAPM Summer School: Specification, Acceptance Testing and Quality Control of Diagnostic X-ray Imaging Equipment* 1991.
95. Melles Griot Optics guide. Vol. 5, Chapters 17-21, 1991.
96. Stanton L, Day JL, Villafana T, Miller CH, Lightfoot DA. Screen-film mammographic technique for breast cancer screening. *Radiology* 1987; 163:4771-9.
97. Goodman LR, et al. Digital and conventional chest images:observer performance with film digital radiography system. *Radiology* 1986; 158:27-33.
98. Hanley JA, McNeil BJ. The meaning and the use of the area under a receiver operating characteristic (ROC) curve. *Radiol* 1982; 143:29-36.
99. Hanley JA, McNeil BJ. A method of comparing the areas under receiver operating characteristic curves derived from the same cases. *Radiol* 1983; 148:839-843.
100. Kelsey CA, Mettler FA. ROC analysis can reveal best diagnostic method. *Diagnost Imag* 1989; 155-161.
101. McNeil BJ, Hanley JA. Statistical approaches to the analysis of receiver operating characteristic (ROC) curves. *Med Decis Making* 1984; 4:137-150.
102. Metz CE. ROC methodology in radiologic imaging. *Invest Radiol* 1986; 21:720-733.
103. Swets JA. ROC analysis applied to the evaluation of medical imaging techniques. *Invest Radiol* 1979; 14:109-121.
104. Swets JA, Pickett RM. Evaluation of diagnostic systems: methods from signal detection theory. New York: Academic Press 1982.
105. Rockette HE, Gur D, Cooperstein LA, Obuchowski NA, King JL, Fuhrman CR, Tabor EK, Metz CE. Effect of two rating formats in multi-disease ROC study of chest images. *Invest Radiol* 1990;25:225-29.

106. Gur D, Rockette HE, Good WF, Slasky BS, Cooperstein LA, Straub WH, Obuchowski NA, Metz CE. Effect of observer instruction on ROC study of chest images. *Invest Radiol* 1990;25:230-34.
107. Rockette HE, Obuchowski NA, Gur D. Non-parametric estimation of degenerate ROC data sets used for comparison of imaging systems. *Invest Radiol* 1990;25:835-37.
108. Rockette HE, Gur D, Metz CE. The use of continuous and discrete confidence judgments in Receiver Operating Characteristic studies of diagnostic imaging techniques. *Invest Radiol* 1992;27:169-172.
109. Caldwell CB, Yaffe MJ, "Development of an anthropomorphic breast phantom", *Med Phys* 1990; 17(2): .
110. Screen film mammography: Imaging considerations and medical physics responsibilities, Ed. by Gary Barnes and G. Donald Frey, Medical Physics Press, Madison, WI, 1991.
111. AAPM Report No. 29: Equipment requirement and quality control for mammography, Ed. by M. J. Yaffe et al, Published for the American Association of Physicists in Medicine by the American Institute of Physics.
112. Good WF, Maitz GS, Gur D. Joint photographic experts group (JPEG) compatible data compression of mammograms. *J Digi Imag*, 1994; 7(3): 123-132.
113. Shaw CC, Herron JM, Wang T, Breitenstein D. High-resolution storage phosphor imaging with reduced laser beam spot size in image readout. Abstract in *Radiology*, 1994; 193(P): 251.

*\* For convenience, this reference list was adopted from the original proposal. However, the list has been updated and several new references were added. It should be noted that not all references are cited in this report.*

## **APPENDIX I**

### **SPECIFICATIONS FOR THE RESOLUTION TEST PATTERN** **(Nuclear Associates, Model 07-553)**

Figure 1 is an enlarged contact radiograph of the test plate. The spacing of the bar pattern varies in steps between the index marks. For example, the spatial frequency of the pattern between AB is one-half line pair per millimeter and the spatial frequency between CD is 0.85 line pairs per millimeter.

Table #1 tabulates the spatial frequency associated with each of the index marks. A larger line separates the pattern into a group of line pairs with longer lines corresponding to groups of 0.5, 1, 2, 5 and 10 line pairs per millimeter.

Fig. 1

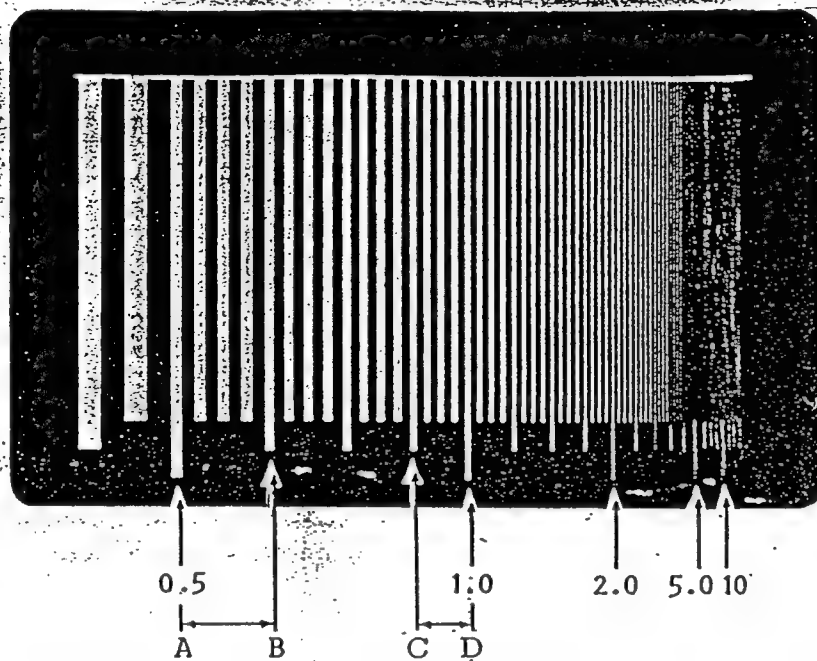


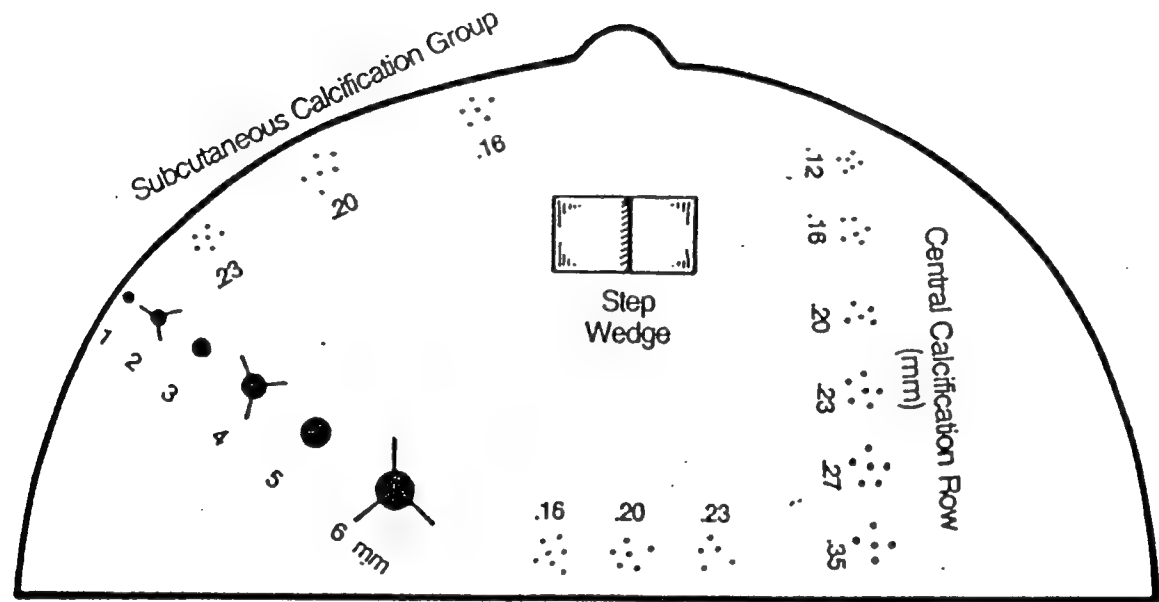
Table #1 The line pairs/mm value for each resolution group is listed below.

Group	LP/mm					
1	0.25	7	1.2	13	3.5	19 <u>10</u>
2	<u>0.5</u>	8	1.4	14	4.2	20 8.5
3	0.6	9	1.7	15	<u>5.0</u>	21 7
4	0.7	10	<u>2.0</u>	16	6	22 6
5	0.85	11	2.4	17	7	
6	<u>1.0</u>	12	2.9	18	8.5	

## APPENDIX II

### **SPECIFICATIONS FOR THE CIRS BREAST PHANTOM** **(Computerized Imaging Reference Systems, Inc.)**

# Map of Embedded Details in Phantoms.



- **Stepwedge**  
5 mm glandular equivalent/5 mm fat equivalent
- **Microcalcifications ( $\text{CaCO}_3$ )**  
12 groupings with largest at .35 mm diameter and smallest at .12 mm diameter. This range of sizes has been shown in practice to be sensitive to system calibration and performance.

- **Masses**  
6 simulated tumor masses ranging from 6 mm diameter to 1 mm diameter
- **Fibrils**  
3 fibre spiculations

**CIRS** COMPUTERIZED IMAGING  
REFERENCE SYSTEMS, INC.

2488 Almeda Avenue, Norfolk, Virginia 23513  
Tel: (804) 855-2765

## **APPENDIX III**

### **SPECIFICATIONS FOR THE CIRS BREAST PHANTOM (Computerized Imaging Reference Systems, Inc.)**

## APPENDIX IV

### CAPTIONS FOR FILMS

Film 1 Storage phosphor image of a resolution test pattern (Nuclear Associates, Model 07-553) acquired with a high resolution storage phosphor screen and scanned with the modified storage phosphor image reader with a reduced beam spot size of 40 $\mu$ m and a pixel size of 43 $\mu$ m. Notice that the 10 lps/mm bars are clearly rendered. The horizontal resolution is slightly better than the vertical one. The image shows much better spatial resolution than those obtained with commercial storage phosphor imaging systems.

Film 2 Storage phosphor image of a resolution test pattern (Nuclear Associates, Model 07-553) acquired with a 14"x17" standard resolution storage phosphor screen and scanned with a commercial storage phosphor image reader (KESPR, Eastman Kodak Company). The pixel size is 173 $\mu$ m. Notice that bar pattern is resolved at up to 2.4 lps/mm. Although there is ample contrast, serious aliasing effects are present at frequencies above 2.4 lps/mm.

Film 3 Storage phosphor image of a resolution test pattern (Nuclear Associates, Model 07-553) acquired with a 8"x10" high resolution storage phosphor screen (Fuji HRIII-n) and scanned with a commercial storage phosphor image reader (KESPR, Eastman Kodak Company). The pixel size is 100 $\mu$ m. Notice that bar pattern is resolved at up to 5 lps/mm. Although there is some contrast, serious aliasing effects are present at frequencies above 5 lps/mm.

Film 4 Storage phosphor image of a CIRS breast phantom acquired with a high resolution storage phosphor screen (Fuji HRIIIIn) and scanned with the improved storage phosphor image reader. The x-ray techniques used are identical to those used in obtaining the screen-film image in Film 5. Notice that most calcifications (with a diameter of 8 mils or greater) and masses (with a diameter of 2 mil (50  $\mu$ m) or greater) are well resolved.

Film 5 Screen-film image of the specially designed wire phantom acquired with grids at 25 kVp and 208 mAs. The screen-film image shows the calcifications, masses and fabrils with a sharper appearance which is partially due to its smaller (by a factor of 2) format. However, it does not resolve more than what can be resolved in the storage phosphor image. This shows that at typical clinical exposure level (as determined by the automatic exposure control), the improved storage phosphor imaging system approaches the conventional screen-film combinations in quality as far as detection of microcalcifications and masses is concerned.

Film 6 Storage phosphor image of the specially designed wire phantom acquired with a high resolution storage phosphor screen (Fuji HRIIIIn) and scanned with the improved storage phosphor image reader. The x-ray techniques used are identical to those used in obtaining the screen-film image in Film 7. Notice that the 5 mil (125 $\mu$ m) wire segments are well resolved while the 4 mil (100 $\mu$ m) wire segments are marginally resolved. All but the 2 mil (50  $\mu$ m) long wires (oriented in radial direction) are resolved.

Film 7 Screen-film image of the specially designed wire phantom acquired with grids at 25 kVp and 26 mAs. The screen-film image shows the wire segments with a sharper appearance which is partially due to its smaller (by a factor of 2) format. This helps resolve the 4 mil (100 $\mu$ m) wire segments. However, it does not resolve finer segments (2, 3 mil) or wires (2 mil). This shows that at typical clinical exposure level (as determined by the automatic exposure control), the improved storage phosphor imaging system approaches the conventional screen-film combinations in quality as far as detection of microcalcifications is concerned.

Film 8 Storage phosphor image of the multiple window meat phantom designed for image acquisition in this project. Groups of five calcifications (simulated by 4, 5 or 6 mil aluminum wire segments) are present in selected window #2, 3, 5, 7, 8, 9, 10, 11 and 12. 5 and 6 mil calcifications are largely visible with different degrees of difficulty, depending on the background structures. 4 mil calcification are generally difficult or impossible to visualize.

Film 9 Min-R screen-film image of the multiple window meat phantom designed for image acquisition in this project. Notice that the aluminum wire segments (to simulate calcifications) have a sharper appearance in the screen-film image. This increases the ease for the 5 and 6 mil calcifications to be seen. However, 4 mil calcifications (in window #3 and 5) are still difficult to detect though perhaps not impossible.

## **APPENDIX V**

**"Joint Photographic Experts Group (JPEG) Compatible Data  
Compression of Mammograms"**

**by Walter F. Good, Glenn S. Maitz, David Gur**

**Department of Radiology, University of Pittsburgh  
Pittsburgh, Pennsylvania 15261**

**Published in Journal of Digital Imaging, Vol 7, No 3, 1994: pp 123-132**

## Joint Photographic Experts Group (JPEG) Compatible Data Compression of Mammograms

Walter F. Good, Glenn S. Maitz, and David Gur

We have developed a Joint Photographic Experts Group (JPEG) compatible image compression scheme tailored to the compression of digitized mammographic images. This includes a preprocessing step that segments the tissue area from the background, replaces the background pixels with a constant value, and applies a noise-removal filter to the tissue area. The process was tested by performing a just-noticeable difference (JND) study to determine the relationship between compression ratio and a reader's ability to discriminate between compressed and noncompressed versions of digitized mammograms. We found that at compression ratios of 15:1 and below, image-processing experts are unable to detect a difference, whereas at ratios of 60:1 and above they can identify the compressed image nearly 100% of the time. The performance of less specialized viewers was significantly lower because these viewers seemed to have difficulty in differentiating between artifact and real information at the lower and middle compression ratios. This preliminary study suggests that digitized mammograms are very amenable to compression by techniques compatible with the JPEG standard. However, this study was not designed to address the efficacy of image compression process for mammography, but is a necessary first step in optimizing the compression in anticipation of more elaborate reader performance (ROC) studies.

Copyright © 1994 by W.B. Saunders Company

**KEY WORDS:** Data compression, mammography, Joint Photographic Experts Group (JPEG), image processing, picture archiving and communication system.

**I**N RECENT YEARS, there has been a rapid increase in the use of mammography and a corresponding increase in the complexity of managing mammographic studies. Many believe that to accommodate the large number of mammographic studies now being performed, these images must be managed in a digital format. The main difficulty with this relates to the large volume of digital data needed to represent each image. High-resolution digital mammograms are likely to contain 10 to 40 Mbyte each. Digital-archiving and data-transmission systems quickly become strained when called upon to deal with a large number of these images. The application of image-compression techniques has the potential to greatly reduce this problem.

Because the problems of dealing with digital image data are universal, the Joint Photographic Experts Group (JPEG) has recently

defined a general-purpose image-compression standard.<sup>1-3</sup> Because the JPEG standard does not specifically address mammographic images, our aim in this study was to develop a compression technique for digitized mammograms which is compatible with the standard, but which is optimized for mammographic images, and then to determine the level of compression that can be achieved before the effects of compression become detectable by observers.

The JPEG algorithm is a block quantization version of the cosine transform in which images are divided into 8- × 8-pixel blocks and the cosine transforms applied to each block individually. The frequency coefficients calculated from the cosine transform are quantized by dividing by values from an array of quantization factors and rounding the quotients to integral values. The resulting array of quotients is aligned in a zigzag order and then encoded by either Huffman coding or by adaptive arithmetic coding. In this method, the quantization factors that are applied to the frequency coefficients determine the compression ratio as well as the kind of information lost or artifact introduced.

The main challenge in applying JPEG standard compression relates to the need to tailor the technique to the characteristics of the particular kind of images being compressed. There are two main areas where there is flexibility in applying the standard—in the quantization of the frequency coefficients and in preprocessing the image before the application of the JPEG algorithm.

In the past, most attention has focused on the

---

From the Department of Radiology, University of Pittsburgh, Pittsburgh, PA.

Supported in part by Grant No. DAMD 17-93-J3009 from the Department of the Army. The content of the information included in this manuscript does not reflect the position or the policy of the government and no official endorsement should be inferred.

Address reprint requests to Walter F. Good, PhD, A439 Scaife Hall, Department of Radiology, University of Pittsburgh, Pittsburgh, PA 15261-0001.

Copyright © 1994 by W.B. Saunders Company  
0897-1889/94/0703-0007\$3.00/0

design of the quantization table required in the quantization stage of the compression process. The default quantization factors, which are provided in the standard, are not adequate for most purposes—hence, the standard encourages user-specified quantization tables. But the resulting image quality is determined by the quantization table used, so the design of these tables must be optimized for the particular compression task.

The current trend is to base quantization tables on psychophysical consideration.<sup>4-6</sup> This approach is somewhat controversial when the compression is to be used for radiographic images, because psychophysical compression techniques assume prior knowledge of display characteristics and viewing conditions. The most common alternative is to use uniform quantization. The justification for this rests on the assumption that there is no a priori reason to believe that certain spatial frequencies are more important than others.

In our interpretation, the JPEG standard implies that any compression process is compatible with the standard if the encoded images it produces can be decoded with a standard JPEG decoder. Specifically, this permits various kinds of preprocessing to be applied to the input image data before the actual compression. Such preprocessing can improve the overall results of the compression/decompression cycle. For example, we have shown<sup>7</sup> that when root mean square error (RMSE) is used as the measure of image fidelity, at sufficiently large compression ratios, there are significant advantages to applying a noise-removal filter to the image data before compression.

Another aspect of this preprocessing, which is somewhat unique to mammography, involves the segmentation of the image. Much of the area in a typical digitized mammogram corresponds to background pixels rather than to tissue pixels. These background pixels contain noise that is typically difficult to compress. To optimize compression in this case, it is important to minimize the amount of data required to represent these background pixels in the encoded image. This can be done in a JPEG-compatible manner by first cropping the image to the smallest rectangular area that contains all of the tissue, and then identifying the remaining background pixels and replacing them with a constant value.

With these considerations in mind, in our laboratory we have developed and begun testing software for JPEG-compatible compression of digitized mammograms.

#### MATERIALS AND METHODS

As described in more detail below, our compression software is consistent with the extended 12-bit version of the JPEG standard and uses a set of preprocessing routines designed specifically for mammograms. This software was written in C to be transportable, but all of the processing reported in this paper was performed on a standard 33-MHz 486 personal computer. We have tested this software by using it to compress a set of digitized mammograms at various levels of quantization, and then evaluating the quality of these compressed images by performing a just-noticeable difference (JND) study.

*Preprocessing.* Before applying the JPEG compression algorithm, the image data is preprocessed to improve its compressibility. This preprocessing operation is divided into two phases; first the image is segmented and cropped and the background pixel values are modified to minimize the storage requirements for the background, and then a noise-removal filter is applied to the tissue pixels.

We begin the segmentation process by automatically determining a threshold value from the histogram of the digitized source image that indicates the transition between background values and tissue values. This threshold value is used to classify pixels in the image as either tissue or background so as to produce a two-valued mask corresponding to the tissue-background separation. The thresholded image normally consists of a large contiguous region corresponding to tissue, possibly containing small holes, as well as smaller isolated clusters of points from the noisier background regions.

An initial "seed" point in the tissue area is automatically selected and grown to encompass the largest possible connected region. This produces a binary mask matching the tissue pixels in the source image. This mask is expanded by 15 pixels—ie, any pixel that is within 15 pixels of a tissue pixel is appended to the mask. This expansion is effected by convolving the binary mask with a 31- × 31-pixel uniformly weighted kernel and then assigning all nonzero pixels the value 1.

We then convolve this binary mask with a 17- × 17-pixel uniformly weighted kernel to smooth the edge between the mask (pixels = 1) and background (pixels = 0). This expanded and smoothed mask, whose pixel values represent an interpolation factor  $\lambda$ , has a value of 1 for every soft-tissue pixel and every background pixel within 7 pixels of a tissue pixel, and goes smoothly to zero over a distance of 16 pixels as the distance from tissue pixels increases. This mask and the source image are both cropped to a rectangular area that excludes as many zero pixels as possible while retaining all nonzero pixels.

A constant value, which is to be used in modifying background pixels, is determined by averaging the background pixels that are near the skin boundary. Finally, the output image is created pixel by pixel by interpolating between the source image and the constant value using the

formula

$$\text{output} = \lambda \cdot \text{source} + (1 - \lambda) \cdot \text{constant} \quad (1)$$

The resulting image has the following characteristics: (1) any 8- × 8-pixel block that contains a tissue pixel will remain unchanged from the source image, eliminating the possibility that the segmentation process will alter the effect of compression on any tissue pixel; and (2) background pixels will have been modified to change in a smooth and continuous manner from their original values to the prescribed constant value as a function of distance from the nearest tissue pixel, thus reducing the possibility that the segmentation process will introduce an edge artifact at the tissue/background boundary.

The second preprocessing phase involves the application of a filter to the tissue area of the image. The particular filter tested here is a nonlinear order filter<sup>7,8</sup> that was designed to modify mainly pixels with large noise components while leaving the majority of pixels unchanged. This filter operates as follows. The source image is first decomposed into a high-frequency component and a low-frequency component by unsharp masking—a process whereby a low-frequency version of the source image, obtained by smoothing the source, is subtracted from the source image to produce an edge-enhanced (high-frequency) version of the source. Pixel values in each 3- × 3-pixel block of the high-frequency component are sorted. If the center pixel of the block is the highest value in the block, it is assigned the value of the next lower pixel. Similarly, if it is the lowest value, it is assigned the next higher value. Otherwise, the pixel is left unchanged. This results in a rather innocuous process of eliminating one pixel maxima or minima from the high-frequency component, while leaving most pixels unchanged. The small number of pixels changed are likely to represent noise, as their values are either greater or less than the values of all their immediate neighbors. Microcalcifications in the image are generally preserved because they rarely consist of a single pixel. Finally, the filtered high-frequency component is added back to the low-frequency component to produce the filtered source image.

These preprocessing operations require two convolutions with uniform kernels, two applications of a threshold, a region growing step, an interpolation step, and application of the nonlinear filter. In our implementation, which does not require manual intervention, all of these steps are performed in approximately one third of the time of the compression itself.

*Image compression.* The JPEG compression algorithm used in this study is a software package written and tested in our laboratory that implements the 12-bit version of the extended JPEG standard. For this study, Huffman encoding was used to encode the quantized coefficients and all compression ratios were based on this. The Huffman tables were derived from the statistics of each individual quantized image rather than on the ensemble statistics. Signaling information was not included in the code size when calculating compression ratios.

Results reported in this paper are based on uniform quantization of the frequency coefficients. As discussed below, any quantization scheme that preferentially degrades the high-frequency components (ie, most of the

psychophysical quantization schemes) may be contraindicated in the compression of mammographic images.

*Evaluation of image-compression technique.* In an effort to understand the viability of the methods described above, we carefully selected eight high-quality cases that spanned the range of image characteristics customarily encountered in mammography, with some preference being given to images containing subtle pathology. These cases were digitized and the digital data was compressed over a wide range of compression ratios by applying the above techniques.

The digitization process used a high-resolution, high-contrast sensitivity laser film digitizer (Lumisys, Sunnyvale, CA) that produces a scan matrix of 4,000 × 5,000 pixels for an 8- × 10-in film by digitizing at a 50-μm sampling interval. This pixel resolution results in a Nyquist spatial frequency of 10 cycles/mm, which preserves the signal resolution of the analog film. The modulation transfer function (MTF) at the Nyquist frequency is 30% in the fast-scan direction and 38% in the slow-scan direction. The 16-bit A/D converter of the digitizer permits a density measurement with an RMSE of less than 0.01. This represented less than one third of the noise present in the conventional film at densities exceeding 0.4.

Each digitized image was compressed at five different compression ratios. Because it is the degree of quantization rather than the compression ratio itself that determines the degradation of an image by compression, the quantization factor was used as an independent variable and not the actual compression ratio. The five quantization factors we applied were 40, 60, 80, 100, and 120, which produced average compression ratios between 15:1 and 60:1. The lowest quantization factor is at a level below which it is not expected that one could detect any effect. The highest quantization factor produced a mean compression ratio of 60:1, which is higher than what is required to permit the efficient handling of mammographic images with current digital technology, and it is in the range where studies of other algorithms applied to other image types have shown significant deterioration in image quality.<sup>9,10</sup> Note that these particular quantization factors are only appropriate for images digitized at the resolution and with the noise characteristics under consideration in this study.

All images used in this study, both the compressed versions as well as the original digitized data, were printed on film with a laser film printer (Eastman-Kodak, Rochester, NY). These laser-printed films were used for all image comparisons. It was not possible for us to perform a meaningful comparison of the laser-printed images to the original (nondigitized) images because our laser printer was only capable of printing at a pitch of ~80 μm/pixel, and this resulted in substantial (1.6 ×) magnification of the laser-printed images. However, comparing two images that have both been enlarged to the same degree is possible, and if the enlargement had any effect, we believe it would have been to make it easier for readers to discriminate between noncompressed images and compressed images. The overall digitizer-processor response was calibrated to accurately duplicate the densities and contrast in the original film. Noise contributed by the laser printer is substantially less than image noise caused by quantum mottle and film granularity in the original film.

**Table 1: The Effect of Image Segmentation on Tissue Block Representation (bits per block)**

Image	% of Area Representing Tissue	Bits per Tissue Block (no preprocessing)	Bits per Tissue Block (after segmentation)	Improvement Factor
1	51.1	8.6	30.1	3.5
2	52.9	8.5	27.0	3.2
3	70.5	9.1	32.3	3.5
4	71.7	10.0	28.0	2.8
5	72.4	9.4	23.6	2.5
6	56.8	7.6	26.5	3.5
7	70.7	24.2	27.4	1.1
8	67.0	18.0	22.2	1.2

From the eight originals, which had each been compressed at five compression ratios, a set of 40 randomized pairs of images, each consisting of one laser-printed noncompressed image and one compressed version of the original, were assembled. Readers were asked to view the pairs side by side and were forced to choose the image they believed to have been compressed. Readers were allowed to spend as much time as desired on each pair. The reading environment was equivalent to that normally used for reading mammograms and readers were permitted to use magnifying lenses.

Altogether, 20 readers participated in these readings. They included radiologists experienced in mammography as well as physicists and engineers specializing in medical imaging.

## RESULTS

The performance of our compression system is somewhat image dependent, but for the ensemble of images reported on here, we averaged about 20 s/Mbyte to preprocess and compress source data. Because decompression does not involve any steps similar to preprocessing, we were able to perform it at a rate of 15 s/Mbyte of output data. Although these speeds are not acceptable for a clinical picture archiving and communication system (PACS) environment, we believe they can be easily improved by adopting hardware optimized for the task.

A summary of the impact of image segmentation on the number of bits needed to represent tissue blocks is presented in Table 1. All images included in this table had previously been cropped to a rectangular area whose border was within 1 cm of tissue pixels in each dimension. Column 2 gives the fraction of the cropped image occupied by tissue pixels. Columns 3 and 4 give the average number of bits used to represent each 8- $\times$ 8-pixel block of tissue pixels before and after application of the segmenta-

tion process, for an overall compression ratio in both cases of 40:1. It can be seen from this table that our segmentation process increased the number of bits used to represent each tissue pixel by a factor of 2.7 on the average despite the fact that the background represented only 35.9% of the image area.

From approximately 800 observations in the JND experiment, average observers correctly detected 42%, 55%, 47%, 61%, and 75% of the images for the 15:1, 23:1, 34:1, 45:1, and 60:1 compression ratios, respectively. However, when we looked at the performance of individual readers, we found that there were two readers who were particularly good at making the discriminations required in this study. These readers were a physicist and an electrical engineer who were both specialists in image processing and were familiar with the particular artifacts caused by this type of image compression. These image-processing specialists averaged discrimination rates of 50%, 67%, 75%, 87%, and 100% for the above compression ratios. Their surprising consistency with each other and the monotonic trend of their performance led us to believe that we were actually measuring a meaningful threshold. A plot of the results of this JND study is shown in Fig 1.

## DISCUSSION

*Performance of compression process.* The relationship between the compressibility of tissue, the compressibility of the background, and the relative areas between tissue and background

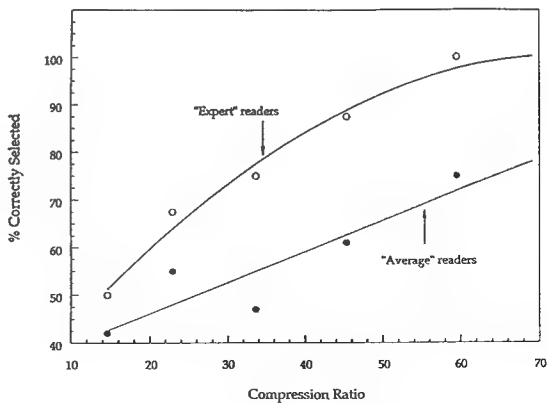


**Fig 1. Performance of image-processing specialists and nonspecialists for the task of identifying compressed versus noncompressed images.**

can be expressed as

$$C_t = \frac{\frac{A_t}{A_t + A_b}}{\frac{C}{C_b}}, \quad (2)$$

in which  $C_t$  and  $C_b$  are, respectively, the compression ratios for  $A_t$  and  $A_b$ , the areas corresponding to tissue and background, and  $C$  is the overall compression ratio for the image. The potential improvement factor in the number of bits per tissue pixel that can be achieved through segmentation, assuming the background is compressed to a negligible size after segmentation, is

$$\frac{1}{1 - \frac{A_b}{A_t + A_b} \cdot \frac{C}{C_b}}, \quad (3)$$

where  $C_b$  is the compression ratio of the background without segmentation. In all cases, after segmentation we were able to compress the background at a ratio of 256:1, which corresponds to using 3 bits to represent each 8- $\times$ 8-pixel block. Theoretically in some unusual cases, it would be possible to use only 2 bits per block, but this is an absolute limit for the JPEG algorithm (sequential discrete cosine transform [DCT] and Huffman encoding). The actual improvements in bits per tissue pixel are indicated in Table 1, column 5.

Note that images 7 and 8 behaved somewhat differently than the other six images. The backgrounds of these images were so dense that they were beyond the range of our digitizer. Consequently, many background pixels values were saturated at the maximum output of our digitizer, and hence, the apparent noise in the background was greatly reduced. Saturation of the background had much the same effect as our segmentation process, but has the potential to also alter tissue pixels in an undesirable way. We have included these particular images after verifying that the tissue pixels themselves were not saturated.

For images 1 through 6, our segmentation process increased the number of bits used to represent each tissue pixel by a factor of 3.2 on the average. If images 7 and 8 are also included, this effect is reduced to 2.7. The average area occupied by tissue pixels in cropped images 1

through 6 was 62.6%. It can be seen that for images in which the background is not saturated, the average improvement in bits per tissue pixel is much larger than what would be suggested simply by the relative areas occupied by the tissue pixels and background pixels.

We illustrate what happens during the segmentation process by using image number 6 from our study as a specific example. This image, which is partially shown in Fig 2, is typical of what we have observed in general. Initially, this mammogram was digitized to a 12.3-Mbyte file. Cropping reduced this by 5.7% to 11.6 Mbyte, and of this file, 56.8% of the pixels corresponded to tissue.

A plot of the compressibility of various regions of this image, which are identified in Fig 2, is presented in Fig 3. The independent variable on this graph, the quantization factor, is specified at the time of compression and directly controls the loss of information during the compression process. It can be seen that different regions of the image vary widely with respect to their compressibility and that the background is significantly less compressible than either of the tissue regions. In many cases such as this one, because the background is very noisy, it is the least compressible part of the image. When the nonsegmented version of this image was compressed at a ratio of 25:1 (0.48 bits per pixel), the compression ratio of the background was only 14.9:1 compared with 51.8:1 (0.23 bits per pixel) for the tissue pixel. The encoded file contained 0.464 Mbyte of data of which 0.337 Mbyte was needed to describe the background and the remaining 0.127 Mbyte represented tissue. In other words, despite the fact that the background was only 43% of the source image, more than 72% of the data in the encoded file was used to describe the background. After the image was preprocessed and compressed at the same 25:1 compression ratio, the constant background in the segmented image was now compressed at a ratio of 256:1 (.05 bits per pixel) and the tissue area was compressed at a ratio of 14.8:1 (0.81 bits per pixel). The background was reduced to only 0.02 Mbyte or about 4% of the encoded data. The net effect was that segmentation increased the amount of data used to represent tissue pixels by a factor of 3.5. Figure 4 compares the overall compress-

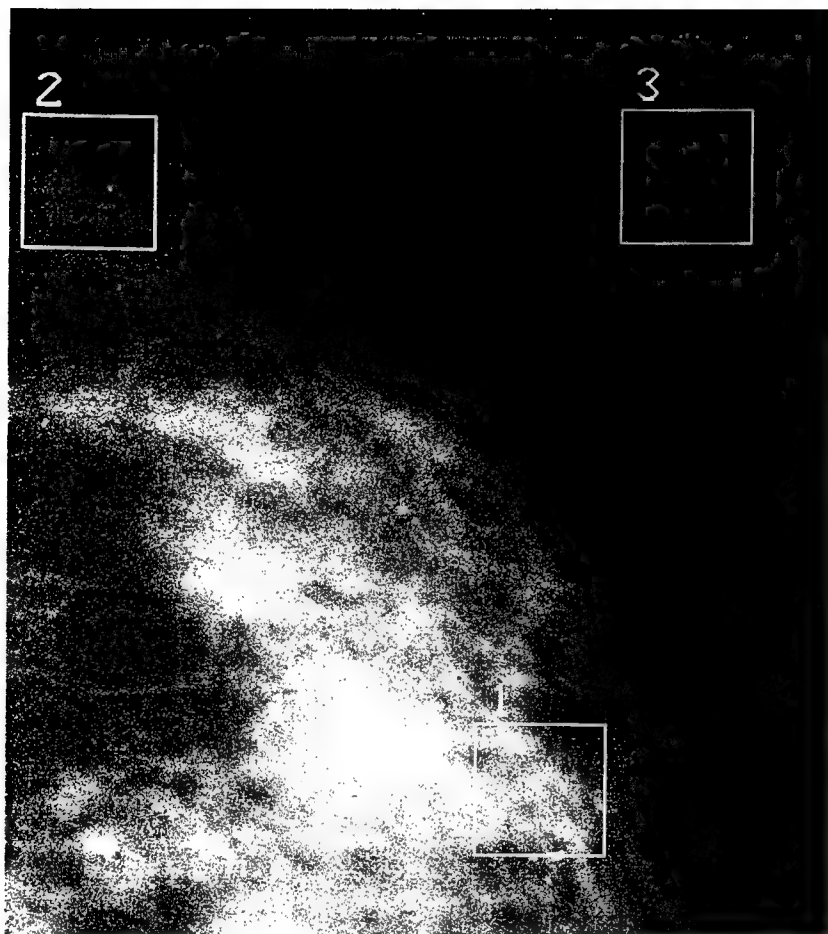


Fig 2. Image showing the three typical regions of interest in different areas representing tissue and background.

ability of the segmented image to that of the nonsegmented image. The compressibility of a chest image is also included for comparison.

Figure 5 shows in more detail the relative number of bits per tissue pixel between the

segmented and nonsegmented images. The actual pattern of the compressibility of various parts of the image is also of interest because it provides information that eventually will be needed for optimizing the relative compression

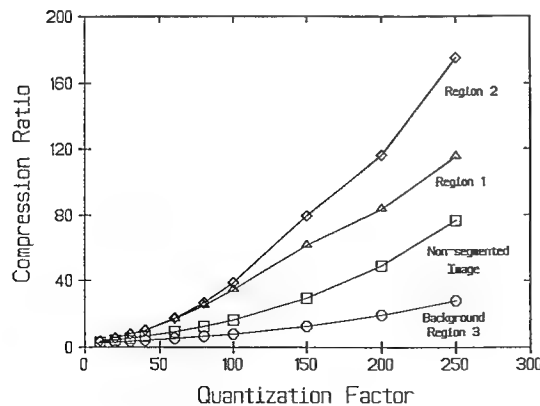


Fig 3. Comparison of the compressibility of the three regions marked in Fig 2, with the compressibility of the image as a whole.

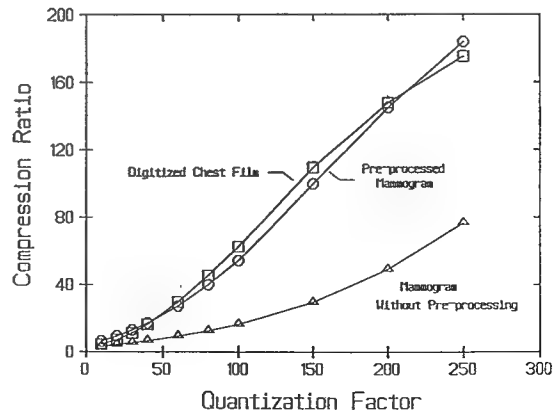


Fig 4. Comparison of the compressibility of mammograms with and without preprocessing to the compressibility of digitized chest images.

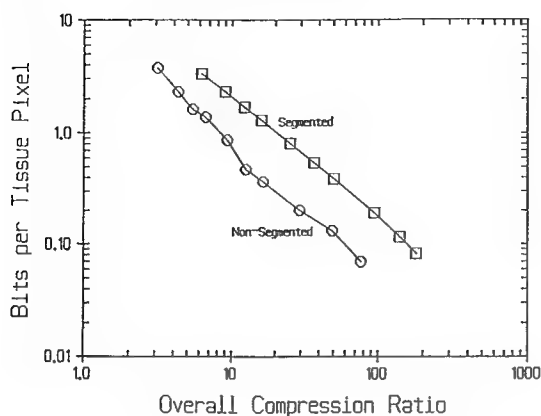


Fig 5. Comparison of the mean number of bits used to represent a tissue pixel for segmented versus nonsegmented images.

of different tissues. Figure 6, A and B show the pattern of bits per pixel with and without preprocessing. It is clear from a comparison of these images that preprocessing results in a dramatic shift, from bits being used to represent background to being used to represent tissue. One further observation from Fig 6B is that a large fraction of the bits used to represent tissue are in fact used to represent only the regions near skin. This observation is consistent throughout the ensemble of images we have studied to date. We believe it is mostly caused by the low compressibility of the high-frequency structures in the near-skin regions and to a lesser extent caused by the high density of the skin areas on the original films that produces increased digitizer noise. This can be seen in Fig 7, which

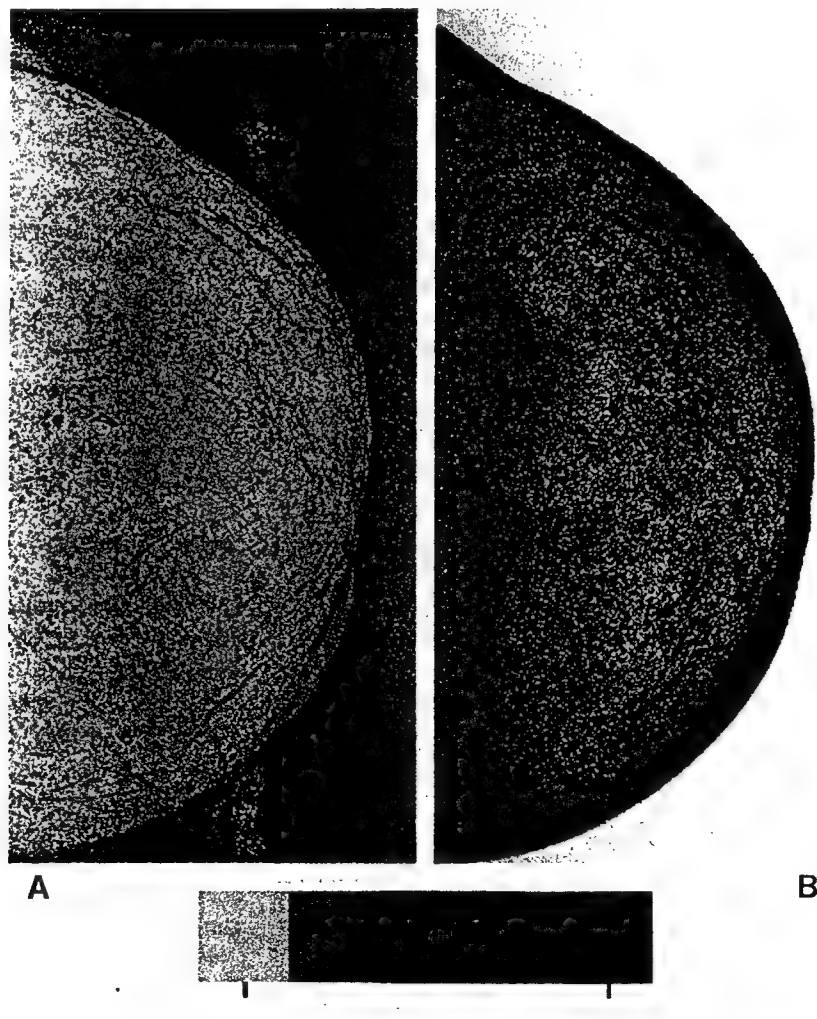


Fig 6. Images of bits per block before segmentation (A) and after segmentation (B) for an image compressed at 40:1.

relates the number of bits per pixel to film density for a fixed quantization level, for reasonably flat areas of an image. The increasing trend as a function of optical density is caused by the increasing noise of the digitizer as film density increases. Also shown in Fig 7 are measurements of the compressibility of skin areas as a function of density. These points are clearly above the line. We have observed that this low compressibility of the skin areas also holds for storage phosphor (computed radiography) images despite the very different noise characteristics of these images.

Future updates to the JPEG standard are likely to contain provisions for adaptive quantization. When this happens, it will be necessary to address the issue of the relative number of data bits that should be allocated to represent each particular type of tissue.

*Effect of filtration.* The effects of applying the nonlinear filter to mammogram number 6 is shown in Fig 8. Although the filter only changed 6.7% of the pixel values, it seemed to provide a net benefit at the higher compression ratios. Its behavior was comparable with what was achieved when a similar filter was applied to the compression of chest images.<sup>7</sup> Figure 8 shows the RMSE for the compression of the filtered source along with the RMSE for the compression of the nonfiltered source as they depend on the compression ratio. It can be seen that at low compression ratios, the RMSE of the filtered image is higher because of changes in the image caused by the filter, but at higher compression

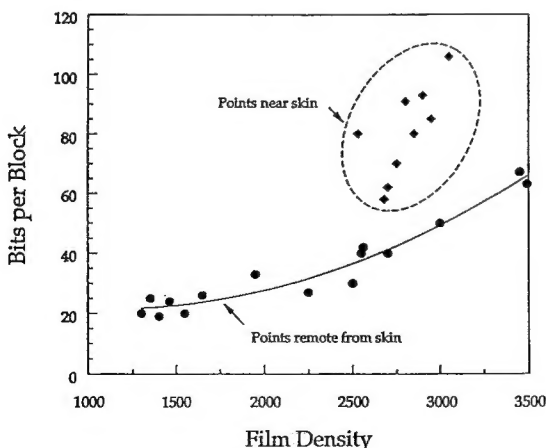


Fig 7. Plot of compressibility of different "nonskin" tissue regions as a function of film density (line). Also included for comparison are data from different points in the skin region.

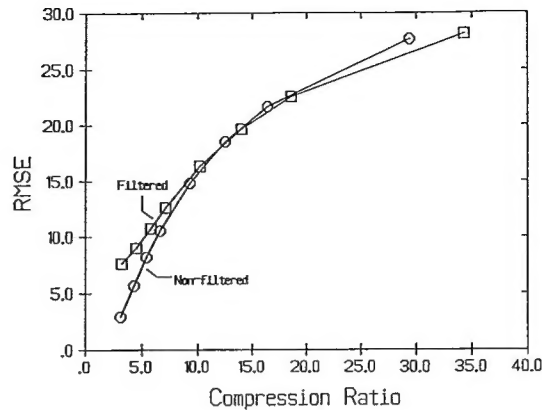


Fig 8. RMSE resulting from nonlinear filtration as a function of compression ratio. Results for both the filtered and nonfiltered image are shown.

ratios, the errors caused by compression overwhelm the error caused by filtration and become predominant. The compression-induced errors are consistently smaller for the filtered image than for the nonfiltered image, and at higher compression ratios, the filtered image actually deviates less from the source image. This behavior persisted across our image set, but was found to be image dependent. It is our view at this time that filtration of this sort is advantageous at compression ratios above 20:1, but it remains to be tested in diagnostic performance studies.

*Effect of segmentation and cropping.* In general, for all of our images, preprocessing the digitized data made a dramatic improvement in compressibility. This improvement can be attributed, for the most part, to the benefit of segmentation. It is actually the degree of compression of the image area corresponding to tissue pixels, or the number of bits per tissue pixel, rather than the compression ratio for the entire image array, that directly determines the impact of compression on the diagnostic quality of mammographic images. In mammography, there is wide variation from case to case in the proportion of the film occupied by tissue pixels. In all cases, after segmentation and cropping, the background will be compressed at a very high compression ratio, whereas the tissue pixels are compressed at a more modest ratio.

If images are not segmented, then cropping is particularly beneficial. However, if the images are segmented by the above procedure, the benefit of cropping is largely neutralized by the

efficiency of the segmentation process in increasing the compressibility of the background. Nevertheless, cropping can be useful, because when the image is reconstructed, it will retain its size before encoding. Maintaining excessive background pixels could have adverse effects on the time required to encode and decode the image as well as on other system components such as image displays.

*Preservation of image quality.* Much of a mammographic image does not contain appreciable high-frequency information, but the need to preserve microcalcifications with dimensions of less than 100  $\mu\text{m}$ , which sometimes appear in mammographic films, may require that we digitize mammograms at 50  $\mu\text{m}$ . This has the effect of oversampling most of the image—ie, the actual information content of the digitized mammogram is much less than the size of the image matrix would suggest.

It does not require severe quantization to achieve a high compression ratio on areas that do not contain high-frequency information. The remainder of the image, such as areas containing microcalcifications or the skin, is not as compressible, but these areas generally comprise such a small fraction of the total area that they have minimal impact on the compression ratio. Together, these factors imply that it may not be necessary or desirable to preferentially degrade the higher-frequency components in the quantization process to achieve high compression ratios, and consequently, it is possible to preserve features such as microcalcifications during the compression process.

In comparing the compressibility of mammograms to that of chest images, we found that preprocessed mammograms are very similar to chest images in compressibility; however, unprocessed mammograms are much more difficult to compress than chest images. We have included a plot in Fig 4 that was derived from a

previous study<sup>7</sup> of the compression ratio of chest images versus the quantization factor. The chest image had been digitized at 100- $\mu\text{m}$  resolution with 12 bits of dynamic range. At each level of quantization, the RMSE for the chest image was similar to the RMSE for mammograms compressed with the same quantization factor.

*Observer performance.* When the differences between images are small, it is possible that readers can detect the difference, but still not be able to tell which image is compressed. The key to differentiating between images at the lower compression ratios seemed to be the presence or absence of blocking artifact. For the compression techniques we applied in this study, blocking artifact becomes noticeable before any degradation of image resolution is obvious. Blocking artifact could be detected by image-processing specialists and nonspecialists alike, but the nonspecialist readers were more likely to misinterpret it. It is clear from discussions with some readers upon completion of their readings, that when the blocking artifact was barely visible they sometimes mistook it for actual image information and assumed the image with the artifact was the noncompressed image. The two best readers seemed to be able to avoid this mistake.

The JND study presented here is not intended to address the question of the impact of compression on diagnostic performance. Its purpose was merely to give us an opportunity to test the feasibility of the techniques we believe are appropriate for the compression of mammographic data, and to identify the range of compression ratios that merit further study. There are many possibilities for further refinements, particularly in the area of preprocessing the data, that are within the constraints of the standard, and these will likely extend the useful range of compression ratios.

## REFERENCES

1. Joint Photographic Experts Group (JPEG): JPEG Technical Specification, Revision 5 (Document No. JPEG-8-R5 or JTC1/SC2/WG8 N933). ISO Central Secretariat, 1990
2. Hudson GP, Yasuda H, Sebestyen I: The international standardization of a still picture compression technique. Proc IEEE Global Telecommunications Conference & Exhibition, vol 2, November 28-December 1, 1988, pp 1016-1021
3. Wallace G, Vivian R, Poulsen H: Subjective testing results for still picture compression algorithms for international standardization. Proc IEEE Global Telecommunications Conference & Exhibition, vol 2, November 28-December 1, 1988, pp 1022-1027
4. Daly S: Application of a noise adaptive contrast sensitivity function to image data compression. Proc SPIE 1077:217-227, 1989
5. Rabbani M, Daly S: An optimized image data compression technique utilized in the Kodak SV9600 still video transceiver. Proc. SPIE 1071:246-256, 1989

6. Ngan KN, Leong KS, Harcharan S: Cosine transform coding incorporating human visual system model. *Proc SPIE* 707:165-171, 1986
7. Good WF, Gur D: Quantization techniques for the compression of chest images by JPEG type algorithms. *Proc SPIE* 1652:114-121, 1992
8. Boncelet CG: Some uses for order statistic filtering in image compression. *Proc SPIE* 1247:51-57, 1990
9. Ishigaki T, Sakuma S, Ikeda M, Itoh Y, Suzuki M, Iwai S: Clinical evaluation of irreversible image compression: Analysis of chest imaging with computed radiography. *Radiology* 175:739-743, 1990
10. MacMahon H, Doi K, Sanada S, Montner SM, Giger ML, Metz CE, Nakamori N, Yin F-F, Xu X-W, Yonekawa H, Takeuchi H: Data compression: Effect on diagnostic accuracy in digital chest radiography. *Radiology* 178:175-179, 1991

ADDENDUM

Copies of microfilm referenced in this report can be obtained from the following addressee:

Chris C. Shaw, Ph.D.  
Department of Radiology  
A441 Scaife Hall  
University of Pittsburgh  
Pittsburgh, Pennsylvania 15261